

Mobile charges in MoS_2 /high- k oxide transistors: from abnormal instabilities to memory-like dynamics

*Shaokai Zhou,^{†,‡} Haihui Cai,^{†,‡} Yehao Wu,^{†,‡} Yufeng Min,^P Renchen Yuan,^P
Yezhu Lv,[†] Jianming Huang,[†] Yuanyuan Shi,^{*,P} and Yury Yuryevich
Illarionov^{*,†}*

*[†]Laboratory of 2D Optoelectronics and Nanoelectronics (L2DON), State Key Laboratory of
Quantum Functional Materials, Department of Materials Science and Engineering,
Southern University of Science and Technology, 1088 Xueyuan Blvd, 518055 Shenzhen,
China*

[‡]These authors contributed equally to this work.

*PSchool of Microelectronics, University of Science and Technology of China, 230026 Hefei,
China*

E-mail: yuanyuansi@ustc.edu.cn; illarionov@sustech.edu.cn

Abstract

MoS_2 field-effect transistors (FETs) with high- k oxides currently lag behind silicon standards in bias and temperature stability due to ubiquitous border oxide traps that cause clockwise (CW) hysteresis in gate transfer characteristics. While suppressing this effect is typically mandatory for logic FETs, here we explore an alternative strategy where the initial CW hysteresis can be dynamically overcome by stronger counter-clockwise (CCW) hysteresis towards memory-like dynamics. We systematically compare hysteresis in similar back-gated $\text{MoS}_2/\text{HfO}_2$ and $\text{MoS}_2/\text{Al}_2\text{O}_3$ FETs up to 275°C.

At room temperature, both devices initially show sizable CW hysteresis. However, at 175°C MoS₂/HfO₂ FETs exhibit dominant CCW dynamics coupled with self-doping and negative differential resistance (NDR) effects. Our compact model suggests that this behavior is caused by the drift of mobile oxygen vacancies (V_O^+ or V_O^{2+}) within HfO₂ which also causes negative V_{th} shift under a constant positive bias stress. This alternative mechanism effectively overrides the initial CW hysteresis and enables intrinsic memory functionality that can be enhanced by using narrower gate bias sweep ranges. In contrast, the MoS₂/Al₂O₃ FETs display only minor CCW dynamics even at 275°C due to higher drift activation energies for the same vacancies, thereby maintaining superior stability. Our results reveal an insulators selection paradigm: Al₂O₃ layers are better suited to suppress detrimental negative V_{th} shifts in MoS₂ logic FETs at high temperatures, whereas their HfO₂ counterparts can serve as active memory layers that would exploit these abnormal instabilities.

Moore's scaling of silicon-based FETs is approaching its fundamental limits due to sizable short-channel effects and mobility degradation in thin Si nanosheets.¹ This creates an urgent need for alternative channel materials such as 2D semiconductors^{2,3} which could replace or substitute Si in next-generation integrated circuits.^{2,4,5} Atomically thin MoS₂ that enables superior electrostatic control and offers reasonable compatibility with conventional high-k oxides such as HfO₂ and Al₂O₃ has emerged as a leading candidate for 2D n-FETs.^{3,6,7} Furthermore, recent research advances^{2,8–11} have made it possible to move forward from lab prototypes to the trial integration of the MoS₂ FETs with HfO₂ and Al₂O₃ into the industrial process lines.^{6,7,12–14} However, these devices still face severe stability and reliability limitations caused by various defects in gate insulators, with border oxide traps^{15,16} and mobile charges^{17,18} being the most ubiquitous. As a result, the pathway of MoS₂ FETs and other 2D devices to the mass-production is delayed since it is still hard to compete with Si technologies in stable long-term operation.

A powerful diagnostic tool to benchmark stable operation of MoS₂ FETs can be offered by comprehensive analysis of time-dependent hysteresis dynamics in the gate transfer (I_D - V_G) characteristics.^{16,17,19,20} Hysteresis serves as a sensitive indicator for the stability of MoS₂ FETs and can also reveal valuable physical phenomena that could be exploited for beyond-FET applications. That is because it directly reflects threshold voltage fluctuations and captures key information about dynamic processes such as charge trapping by oxide defects and drift of mobile charges.¹⁸ However, many existing studies on 2D FETs miss this opportunity to get in-depth information and use just a single sweep at a random sweep rate which only allows to speculate that hysteresis is “negligible” or “near-zero”^{21–24,24–26} with no relation to the real physical picture. As a result, no systematic comparison of time- and temperature-dependent hysteresis dynamics in MoS₂ FETs with HfO₂ and Al₂O₃ insulators under identical conditions can be found in the literature. This prevents clear understanding of intrinsic stability concerns introduced by these two most widely used high-k gate oxides and thus impedes formulation of targeted optimization strategies that could finally enable

MoS_2 /high-k FETs with competitive stability. Furthermore, the lack of detailed studies focused specifically on abnormal CCW dynamics impedes possible ways for the practical use of this phenomena in memory devices as an alternative to suppression.

Here we perform a systematic comparison of hysteresis dynamics in $\text{MoS}_2/\text{HfO}_2$ and $\text{MoS}_2/\text{Al}_2\text{O}_3$ FETs fabricated using identical methods at sweep times up to tens of kiloseconds and temperatures varied from 25°C to 275°C and support our findings with bias stress measurements. Our results reveal that at room temperature both devices exhibit a CW hysteresis that is caused by charge trapping and thus defined by energetic alignment of oxide defect bands. However, at 175°C our $\text{MoS}_2/\text{HfO}_2$ FETs exhibit change of hysteresis to the CCW direction coming together with NDR and self-doping effects. Our qualitative compact model for mobile charges in oxides nicely reproduces the CCW hysteresis with all related phenomena and suggests the drift of positive oxygen vacancies in HfO_2 as the primary reason that may also result in controllable memory-like dynamics. However, in Al_2O_3 insulators similar trends are barely visible even at the temperatures as high as 275°C due to larger migration barriers of the same vacancies, thus making this insulator more suitable to mitigate detrimental negative shifts of V_{th} under the positive bias stress.

Results and Discussion

Investigated devices and measurement technique

We examine back-gated MoS_2 FETs with HfO_2 and Al_2O_3 gate insulators with the schematic layout shown in Fig.1a. To enable consistent comparison of the device stability, for both types of FETs we used single-layer MoS_2 films grown by chemical-vapor deposition (CVD) taken from the same batch and also employed the identical fabrication processes. First, $\text{Ni}(10\text{ nm})/\text{Au}(30\text{ nm})$ local back gate electrodes were created on a pretreated Si/SiO_2 substrate via photolithography and e-beam evaporation. Then a 20 nm-thick HfO_2 or Al_2O_3 insulator was grown by atomic layer deposition (ALD) at 250°C. Next, the MoS_2 film was

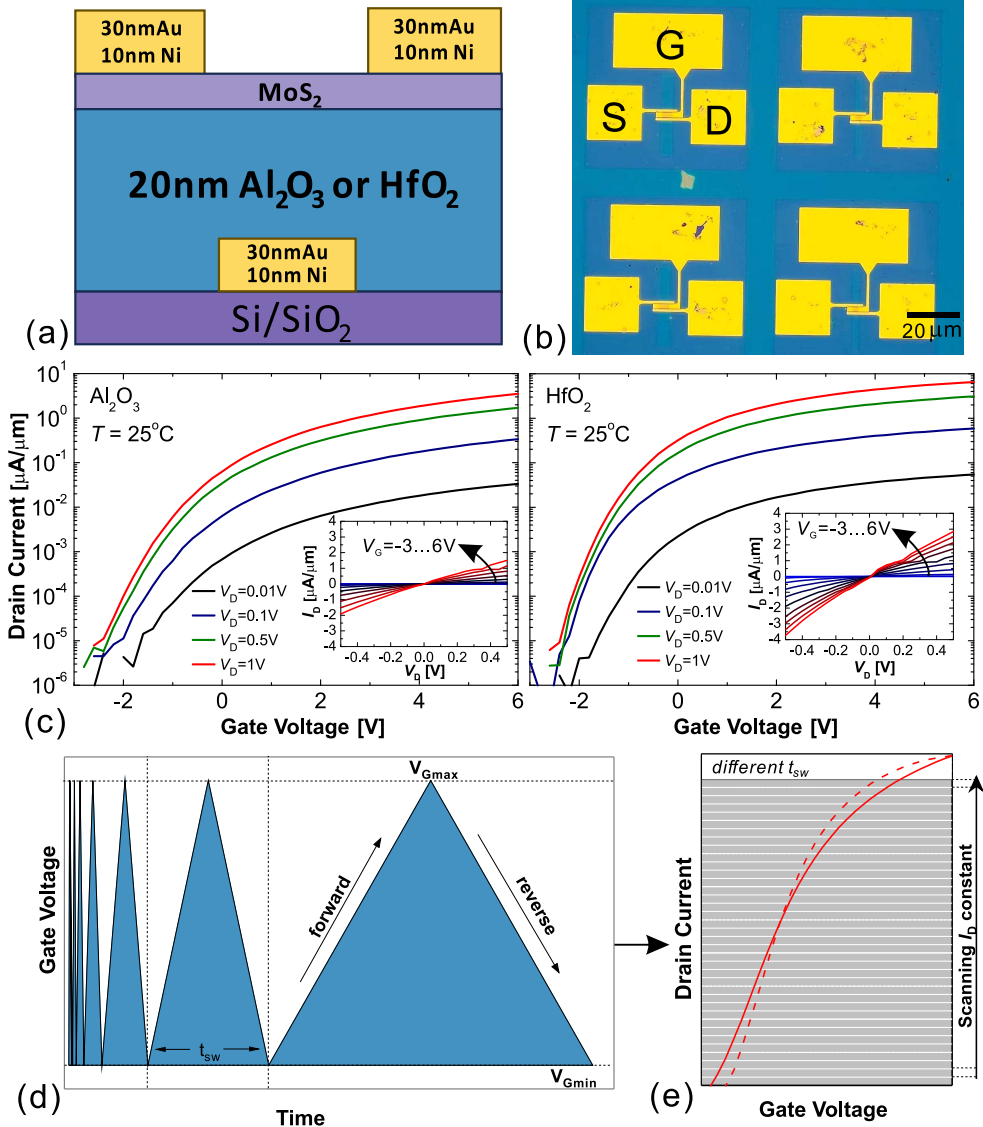


Figure 1: (a) Schematic layout of our back-gated $\text{MoS}_2/\text{HfO}_2$ and $\text{MoS}_2/\text{Al}_2\text{O}_3$ FETs fabricated using the same process. The channel is made of CVD-grown MoS_2 films taken from the same batch. (b) Optical image of four devices inside the array containing tens of FETs. (c) I_D - V_G characteristics of MoS_2 FETs with Al_2O_3 (left) and HfO_2 (right) measured at different V_D . The insets show the corresponding I_D - V_D curves. (d) Schematics of the subsequent V_G sweeps with increased t_{sw} used in our hysteresis measurements. In some measurements maximum t_{sw} that we have reached was above 10 ks. (e) Schematics of our universal mapping method²⁷ which suggests scanning the I_D values to obtain minimum (lower UHF) and maximum (upper UHF) from the extracted family of $\Delta V_H(1/t_{sw})$ curves.

transferred through a wet transfer process, followed by residual removal and patterning of the channel via photolithography and reactive ion etching. Finally, the source/drain electrodes were defined by photolithography and metalized with Ni(10 nm)/Au(30 nm) via e-beam evaporation and lift-off process. The obtained arrays with many tens of MoS₂ FETs of both types (Fig.1b) with channel length L and width W varied between 5 and 100 μm allowed us to perform systematic measurements while verifying the reproducibility of all observed trends.

The electrical characterization of our MoS₂ FETs was performed in vacuum and in complete darkness. First we have checked the $I_{\text{D}}-V_{\text{G}}$ characteristics at different drain voltages V_{D} . As shown in Fig.1c, for both MoS₂/Al₂O₃ and MoS₂/HfO₂ FETs decent performance with on/off current ratios of about 10⁶ is obtained, while the output ($I_{\text{D}}-V_{\text{D}}$) curves also look reasonable. Next we measured the hysteresis using subsequent double sweeps of the $I_{\text{D}}-V_{\text{G}}$ characteristics at $V_{\text{D}} = 0.1 \text{ V}$ with sweep times t_{sw} increased from tens of seconds to over 10 ks (Fig.1d), while repeating the measurements with different V_{G} sweep ranges. For consistent extraction of the hysteresis width ΔV_{H} vs. $1/t_{\text{sw}}$ dependences we used our standardized universal mapping method.²⁷ This approach suggests scanning the constant current value to extract the lower and upper universal hysteresis functions (UHFs),²⁷ as schematically shown in Fig.1e. In contrast to the conventional constant current approach used in our previous studies,^{17,28} the mapping method captures complex hysteresis dynamics like the CW/CCW switching caused by two competing mechanisms such as charge trapping and drift of mobile charges observed in this work.

Hysteresis dynamics at room temperature

First we reveal the impact of gate insulator and device-to-device variability on the hysteresis dynamics at room temperature by examining MoS₂ FETs with different L and W . In Fig.2a we show the double sweep $I_{\text{D}}-V_{\text{G}}$ characteristics measured for 5 MoS₂/Al₂O₃ and 5 MoS₂/HfO₂ devices using the slowest achieved t_{sw} and the V_{G} sweep range of -6 to 6 V. A purely CW hysteresis is observed in all cases. Then we use our full measurement datasets

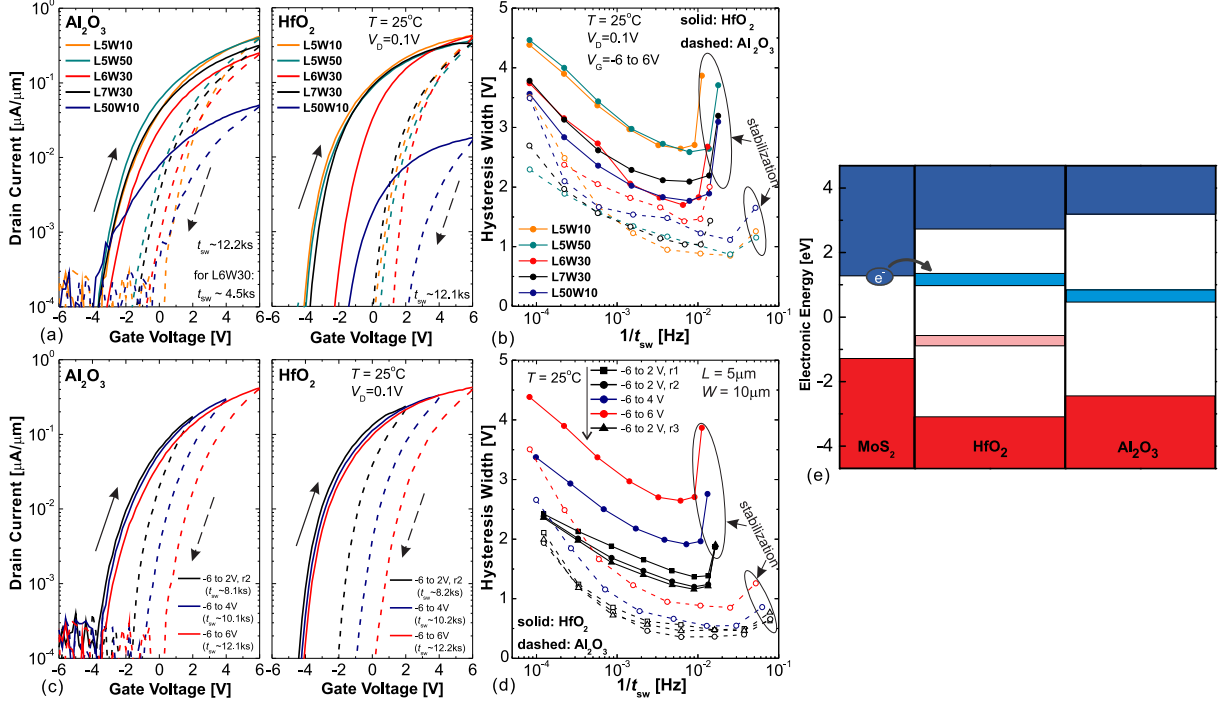


Figure 2: (a) Double sweep I_D - V_G characteristics of 5 MoS₂ FETs with Al₂O₃ (left) and HfO₂ (right) with different L and W measured using the slowest achieved sweeps at 25°C. A purely CW hysteresis is present for all devices. (b) The corresponding ΔV_H vs. $1/t_{sw}$ dependences showing that while there is some device-to-device variability for both types of devices, in overall the CW hysteresis is smaller for the devices with Al₂O₃. (c) Double sweep I_D - V_G characteristics of the representative MoS₂ FETs with Al₂O₃ (left) and HfO₂ (right) measured using the slowest t_{sw} and different V_G sweep ranges. (d) The corresponding ΔV_H vs. $1/t_{sw}$ curves confirm that for the MoS₂/Al₂O₃ FETs hysteresis is smaller for all V_G sweep ranges. Remarkably, the results for -6 to 2 V sweep range repeated in three rounds (r1, r2, r3) in the beginning and in the end of experiment (as illustrated by the arrow next to the legend) show perfect reproducibility. (e) Band diagram showing relative energetic alignments between the conduction band edge E_C of the MoS₂ n-channel and known fundamental defect bands in HfO₂ and Al₂O₃.^{16,29} The upper defect band of HfO₂ is closer to E_C of MoS₂, while the defect band of Al₂O₃ is situated deeper. This explains smaller CW hysteresis in the latter case, since deeper traps in Al₂O₃ get activated at slower sweeps.

consisting of 8 sweeps with t_{sw} ranging between tens of seconds and over ten kiloseconds to perform the full mapping of hysteresis dynamics. As shown in Fig.S1 in the Supplementary Information (SI), for both types of our devices only CW hysteresis is present within the whole range of t_{sw} and thus the $\Delta V_H(1/t_{sw})$ dependences can be consistently expressed with the upper UHFs. In Fig.2b we show the resulting $\Delta V_H(1/t_{sw})$ curves for all 10 devices. While some variability is present within 5 devices of each type, there is no obvious correlation

between the hysteresis magnitude and the channel dimensions. Furthermore, from Fig.2b we can reliably conclude that the CW hysteresis in MoS_2 FETs with Al_2O_3 is generally smaller than in their counterparts with HfO_2 . To get more insights into this difference, we next select representative MoS_2 FETs of both types and measure the hysteresis using different V_G sweep ranges. The double sweep I_D - V_G characteristics measured at the slowest t_{sw} and the corresponding $\Delta V_H(1/t_{\text{sw}})$ dependences are shown in Fig.2c,d, respectively. We can see that for both types of our MoS_2 FETs the CW hysteresis becomes larger for wider V_G sweep ranges and also increases for slower sweeps that is the typical feature of charge trapping by oxide defects.¹⁶ At the same time, it is again reconfirmed that for the $\text{MoS}_2/\text{Al}_2\text{O}_3$ FETs the CW hysteresis is generally smaller and starts to increase at considerably lower sweep frequencies for all three sweep ranges used. Remarkably, the results for the narrowest V_G sweep range of -6 to 2 V measured before and after the use of wider V_G sweep ranges are nicely reproducible. However, stabilizing behavior of the devices which appears as a larger hysteresis measured for the first sweeps of each round has to be noted in all cases.

The observed difference in room temperature hysteresis dynamics between MoS_2 FETs with Al_2O_3 and HfO_2 gate insulators goes in line with the energetic alignment of oxide defect bands with respect to the conduction band edge E_C of MoS_2 as shown in Fig.2e. These defect bands have fundamental positions inside the bandgap of high-k oxides which are relatively well known but may slightly depend on the oxide quality and growth conditions.^{16,29} Namely, the upper defect band of HfO_2 is close to E_C of MoS_2 . This facilitates trapping of electrons from the MoS_2 channel by HfO_2 defects³⁰ which explains a sizable CW hysteresis observed in our $\text{MoS}_2/\text{HfO}_2$ FETs already at faster sweeps. In contrast, the defect band of Al_2O_3 is over 0.5 eV below E_C of MoS_2 , which drastically increases the energy barrier for charge trapping by oxide traps. That is why the CW hysteresis in our $\text{MoS}_2/\text{Al}_2\text{O}_3$ FETs is generally smaller as compared to their counterparts with HfO_2 . Furthermore, ΔV_H starts increasing at smaller sweep frequencies as these deeper traps in Al_2O_3 have larger capture/emission time constants and thus need more time to get activated.

MoS₂/HfO₂ FETs at high temperatures: memory-like performance

Experimental classification of the CCW hysteresis dynamics

In Fig.3a we show the double sweep I_D - V_G characteristics of our MoS₂/HfO₂ FET measured at $T = 175^\circ\text{C}$ using 8 subsequent sweeps with t_{sw} up to 12.1 ks. The corresponding hysteresis mapping results provided in Fig.3b reveal a totally different hysteresis behavior as compared to room temperature. Namely, the hysteresis changes from the CW/CCW switching at fast sweeps to the purely CCW one at slow sweeps. This is followed by sizable increase in the ON state current from one sweep to another (Fig.3a) which suggests progressive n-type doping of MoS₂ during the measurements. Remarkably, our full mapping results clearly separate the frequency regions in which the CW/CCW switching and purely CCW hysteresis are present, as in the former case the upper and lower UHFs are of the opposite signs and in the latter case they are both negative. At the same time, a distinct maximum of the CCW hysteresis is visible. This is in part similar to our previous observations for MoS₂/SiO₂ FETs¹⁷ and hints at the contribution coming from mobile charges in the oxide. Furthermore, in Fig.3c we show the representative I_D - V_G characteristics in linear scale and reveal that for the moderate t_{sw} an NDR effect is present during the reverse sweep. As will be discussed below, this memory-like behavior appears if positive mobile charges approaching the channel side of HfO₂ lag behind V_G changes near $V_{G\text{max}}$. However, for slower t_{sw} a stronger increase of the ON current with no NDR effect is observed because the self-doping peaks at less positive V_G during the forward sweep, and thus by reaching $V_{G\text{max}}$ the charges are already trapped at the channel side of oxide. The related results obtained at $T = 250^\circ\text{C}$ (Fig.3d,e) show that the maximum of CCW hysteresis is shifted towards faster sweeps because of thermal activation of mobile charges. As a result, the CCW contribution becomes smaller at slow sweeps that results in the CW/CCW switching since the charge trapping contribution is still present. However, as the mobile charges are too fast at this temperature, we do not observe any sizable NDR effect. For instance, the inset of Fig.3e suggests that only some signs of the current plateau

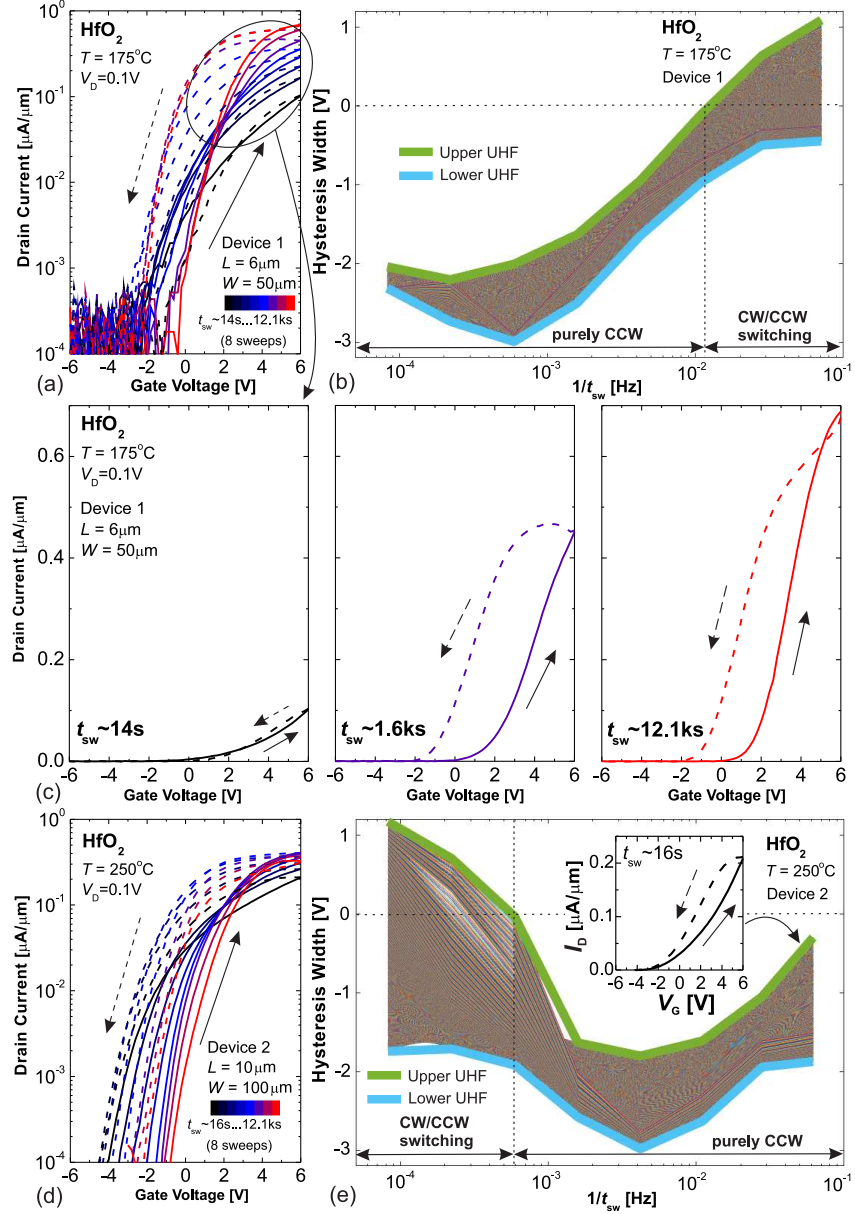


Figure 3: (a) Double sweep I_D - V_G characteristics of our MoS₂/HfO₂ FET measured at $T = 175^\circ\text{C}$ using 8 subsequent sweeps with t_{sw} up to 12.1 ks. The hysteresis dynamics changes from the CW/CCW switching at faster sweeps to the purely CCW hysteresis at slower sweeps. (b) The corresponding mapping results which clearly reveal the frequency ranges of both hysteresis dynamics and a distinct maximum of the CCW hysteresis. (c) Linear scale I_D - V_G curves corresponding to (a) which show development of the CCW hysteresis, i.e. a weak effect at fast t_{sw} , an NDR behavior at moderate t_{sw} and an increase of I_{ON} with localization and decay of the CCW hysteresis at slow t_{sw} . (d,e) The related results measured at $T = 250^\circ\text{C}$. The CCW hysteresis maximum is shifted to faster sweeps and thus the CW/CCW switching is observed at slower sweeps. The inset in (e) highlights that NDR is not observed within the t_{sw} range used since mobile charges are too fast.

are visible in the beginning of reverse sweep even at the fastest t_{sw} used.

We also note that the CCW hysteresis dynamics starts to appear in most our $\text{MoS}_2/\text{HfO}_2$ FETs at $T = 125^\circ\text{C}$ for slow t_{sw} , with some outlying devices with likely more vacancies in the oxide showing NDR behavior already at this temperature. However, $T = 175^\circ\text{C}$ appears to be the optimum for detailed analysis as the CCW hysteresis becomes dominant at this temperature. Furthermore, the observed CCW dynamics are well reproducible between different devices that simplifies analysis if certain devices get failed during the measurements. More detailed results on temperature dependence and reproducibility between different devices can be found in Fig.S2-S3 in the SI.

Understanding the observed trends via compact modeling

To reveal the physical origin of the complex high-temperature hysteresis dynamics in our $\text{MoS}_2/\text{HfO}_2$ FETs, we implement a compact model for the drift of mobile ions in the gate oxide while disregarding the CW contribution coming from oxide traps that is studied elsewhere by considering oxide defect bands.^{17,30} The model incorporates thermally activated hopping of mobile charges with the diffusion coefficient given as

$$D = D_0 \exp\left(-\frac{qE_A}{k_B T}\right) \quad (1)$$

where D_0 is a pre-factor coefficient and E_A is the energy activation barrier for the migration of ions. Following the Einstein relation, this diffusion coefficient sets the mobility of ions and consequently their drift velocity under electric field given by the applied V_G . As a result, the position of mobile charges in the oxide $x(t)$ can be calculated at any time point and used to elaborate the resulting time-dependent threshold voltage shift as

$$\Delta V_{\text{th}}(t) = -\frac{Q_{\text{max}}}{C_{\text{ox}}} \left(1 - \frac{x(t)}{d_{\text{ox}}}\right) \quad (2)$$

where $Q_{\max} = qN_{\text{mob}}d_{\text{ox}}$, N_{mob} is the concentration of mobile charges in the oxide, d_{ox} and C_{ox} are oxide thickness and capacitance, respectively. The minus sign takes into account that we consider positive charges which should create a negative ΔV_{th} that will have a maximum when all ions accumulate near the channel/oxide interface (i.e. $x = 0$). Finally, this ion-induced ΔV_{th} is used for piecewise calculation of the drain current as

$$I_{\text{D}}(V_{\text{G}}, t) = \begin{cases} I_{\text{min}} \cdot \exp\left(\frac{V_{\text{G,eff}} - V_{\text{th}} - \Delta V_{\text{th}}}{SS}\right) & V_{\text{G,eff}} \leq V_{\text{th}} + \Delta V_{\text{th}} \\ \mu_{\text{eff}} \cdot n_{2\text{D}} \cdot q \cdot \frac{W}{L} \cdot V_{\text{D}} & V_{\text{G,eff}} > V_{\text{th}} + \Delta V_{\text{th}} \end{cases} \quad (3)$$

where the carrier density $n_{2\text{D}} = C_{\text{eff}}(V_{\text{G,eff}} - V_{\text{th}} - \Delta V_{\text{th}})/q$ with effective capacitance C_{eff} accounting for the quantum capacitance effects in the MoS₂ channel and the capacitance of interface states. The effective gate voltage $V_{\text{G,eff}} = V_{\text{G}} - Q_{\text{it}}/C_{\text{ox}}$ is used to consider possible screening by interface charges. For simplicity, the subthreshold swing SS, minimum current I_{min} and carrier mobility μ_{eff} were inset as input parameters to the model, and V_{th} was considered to be 0.5 V above the calculated flatband voltage V_{FB} . The use of this approach allowed us to simulate the double sweep $I_{\text{D}}-V_{\text{G}}$ characteristics while considering different t_{sw} . The complete description of our compact model with all parameters can be found in the SI.

We suggest that the CCW hysteresis dynamics that we observe for the MoS₂/HfO₂ devices originate from the drift of positive oxygen vacancies V_O⁺ and V_O²⁺ in HfO₂. Then we have identified that the results of Fig.3 can be qualitatively reproduced with the model by using $E_{\text{A}} = 1.15 \text{ eV}$ which is close to the literature values for oxygen vacancies in HfO₂,³¹ and also physically feasible $N_{\text{mob}} = 3 \times 10^{19} \text{ cm}^{-3}$ and $D_0 = 2 \times 10^{-7} \text{ m}^2/\text{s}$. The simulated double sweep $I_{\text{D}}-V_{\text{G}}$ characteristics which exhibit NDR behavior and the ON current increase are shown in Fig.4a. These results could be interpreted based on the schematics provided in Fig.4b. Namely, at negative V_{G} positive mobile charges are concentrated at the back gate side of HfO₂. As V_{G} becomes positive, they start moving closer to the MoS₂ channel (state 1). Then if t_{sw} is too short for the ions to respond they are far from the channel and thus the

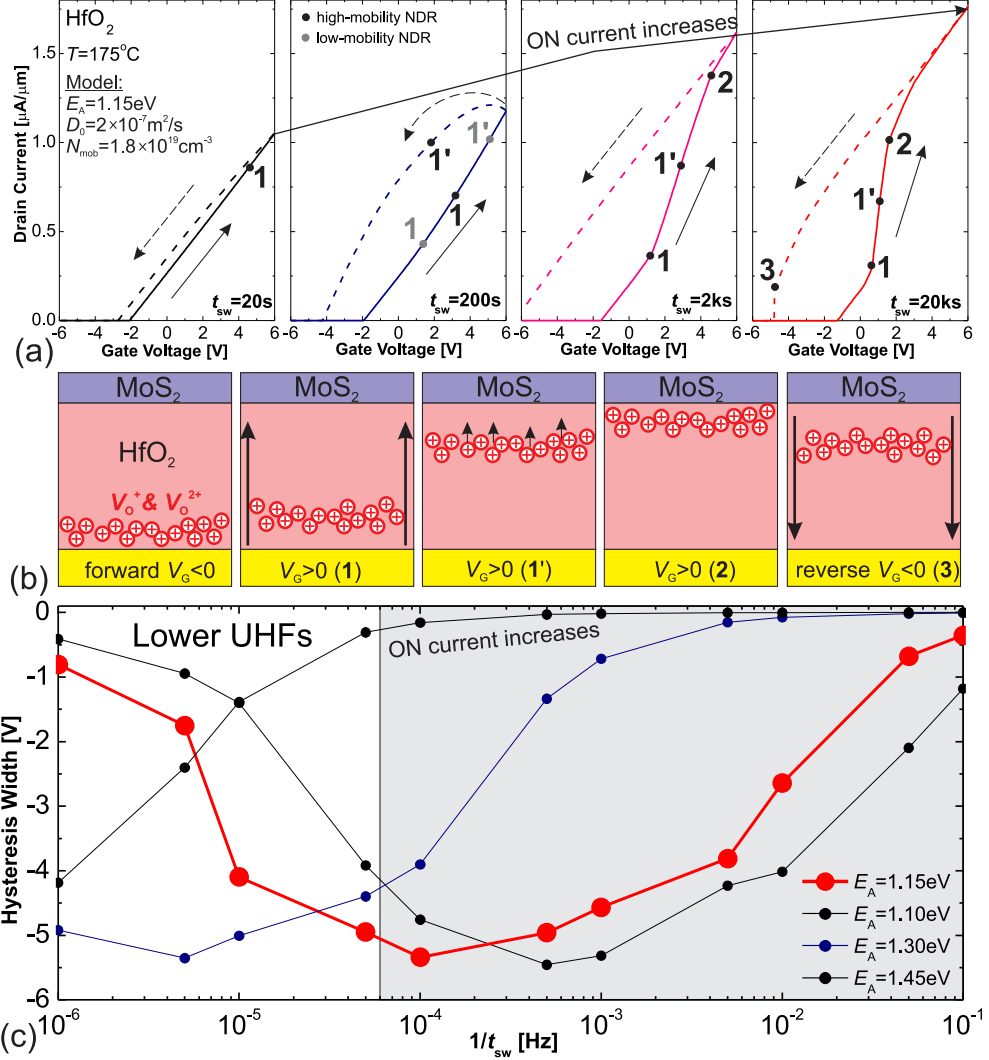


Figure 4: (a) Double sweep I_D - V_G characteristics of the MoS₂/HfO₂ FET simulated with our compact model using different t_{sw} and $T = 175^\circ\text{C}$. The trends are qualitatively similar to our experimental results shown in Fig.3c. (b) Schematics that illustrate the drift of positive oxygen vacancies in the oxide. At negative V_G they are concentrated at the gate side of HfO₂. Then when V_G becomes positive bulk motion towards the MoS₂ channel starts if t_{sw} is slow enough (state 1). However, when approaching MoS₂ the charges start feeling the interface effects and thus slowing down (state 1'), before finally getting trapped at the channel side (state 2). The dynamics of the CCW hysteresis and its side features such as the NDR effect and I_{ON} increase are determined by the relative positions of the points 1, 1' and 2 on the I_D - V_G curves that depend on t_{sw} . Also, if the sweep is too slow, the drift of mobile charges back to the gate may start (state 3) when V_G becomes negative during the reverse sweep. (c) The lower UHFs extracted by mapping method from the series of I_D - V_G characteristics simulated with different E_A . While a maximum of the CCW hysteresis similar to Fig.3b is revealed, a larger E_A shifts it to the slower sweep frequencies and vice versa. The gray box marks typical measurement range.

CCW hysteresis is small. However, for slower t_{sw} the CCW dynamics further develop, as the ions approach the channel making the CCW hysteresis larger, and at the same time start slowing down due to the interface effects (state 1'). In our compact model this is considered by reducing the rate of mobile charges near interfaces (see equation (5) in the SI). Then if V_{Gmax} is within the free bulk motion of ions, i.e. between the states 1 and 1', high-mobility NDR memory effects appear. This is because ions continue moving towards the channel fast when sweep direction changes. As a result I_{D} increases against the V_{G} change as the cumulative ΔV_{th} given by equation (2) becomes more negative. Then the pre-condition for NDR is that mobile charges movement lags behind the V_{G} change. This can be realized also if the state 1' is just before V_{Gmax} as the ions are still moving though much slower, i.e. low-mobility NDR. However, if t_{sw} is increased further, mobile charges finally reach the $\text{MoS}_2/\text{HfO}_2$ interface (state 2) and get trapped there. Then the states 1, 1' and 2 appear already during the forward sweep that causes an abrupt kink of I_{D} instead of NDR. This also results in a sizable increase of I_{ON} due to self-doping with positive charges. However, since at the state 2 all mobile charges are already trapped at the channel side of oxide, they cannot move anymore even if V_{G} increases and thus the CCW hysteresis starts to localize below the point 2. Finally, if the sweep is extremely slow, the state 3 followed by a kink downwards appears at a negative V_{G} during the reverse sweep. This indicates the drift of mobile ions back to the gate side of HfO_2 . Furthermore, as illustrated by our additional simulation results (see Fig.S4 in the SI), the NDR effect is not present if N_{mob} is decreased and becomes more pronounced if it is increased.

In Fig.4c we show the lower UHFs extracted from the $I_{\text{D}}-V_{\text{G}}$ curves simulated using different E_{A} . Just like in Fig.3b,e, a distinct maximum of the CCW hysteresis is present at the sweep frequency roughly corresponding to $1/\tau_{\text{drift}}$ that is required for ions to cross d_{ox} , i.e. if state 2 is reached at V_{Gmax} . At the same time, larger migration barrier obviously shifts the maximum to the slower frequencies and vice versa. In Fig.S5 in the SI we also show that if the pre-factor of the diffusion coefficient D_0 is made smaller, the maximum also moves

to slower frequencies since the ions become slower and need more time to cross the oxide thickness. Based on these observations it is clear that the same hysteresis dynamics could be obtained with different combinations of the three key parameters (see Fig.S6 in the SI). This would obviously make it complicated to use precise fits of the experimental data for extraction of ion parameters. However, we can consider that E_A values which we are using provide a reasonable estimate since any change for more than 0.2 eV would either result in a very different dynamics as compared to our experimental observations, or in non-physical values of N_{mob} and D_0 .

Boosting the NDR magnitude with narrower sweep ranges

Being equipped with fundamental understanding of NDR behavior in our $\text{MoS}_2/\text{HfO}_2$ FETs from the compact model, we next target to confine these memory dynamics by adjusting the V_G sweep range. In Fig.5a we show the double sweep I_D - V_G characteristics of the $\text{MoS}_2/\text{HfO}_2$ FET measured at $T = 175^\circ\text{C}$ using slowest achieved t_{sw} and different V_G sweep ranges. Remarkably, while for the sweep range of -6 to 6 V the CCW hysteresis starts to localize, for the sweeps with smaller $V_{G\text{max}}$ we still observe the NDR effect within this sweep time range. This is a very intuitive observation, since if $V_{G\text{max}}$ is smaller mobile charges need more time to cross d_{ox} and achieve the state 2 shown in Fig.4a,b. The lower UHFs obtained for this and another device provided in Fig.5b indeed confirm that for narrower sweep ranges the maximum of the CCW hysteresis would be reached at considerably slower sweep frequencies. The full hysteresis mapping results for the Device 1 can be found in Fig.S7 in the SI. They particularly illustrate that due to slower drift of mobile charges for the sweep ranges of -6 to 2 V and -6 to 4 V, a purely CW hysteresis caused by charge trapping is still observed for faster sweeps.

In Fig.5c we show the full set of double sweep I_D - V_G characteristics measured using -6 to 4 V sweep range in a linear scale. Remarkably, the magnitude of NDR is considerably stronger as compared to the -6 to 6 V sweep range (e.g. Fig.3). In Fig.5d we show the

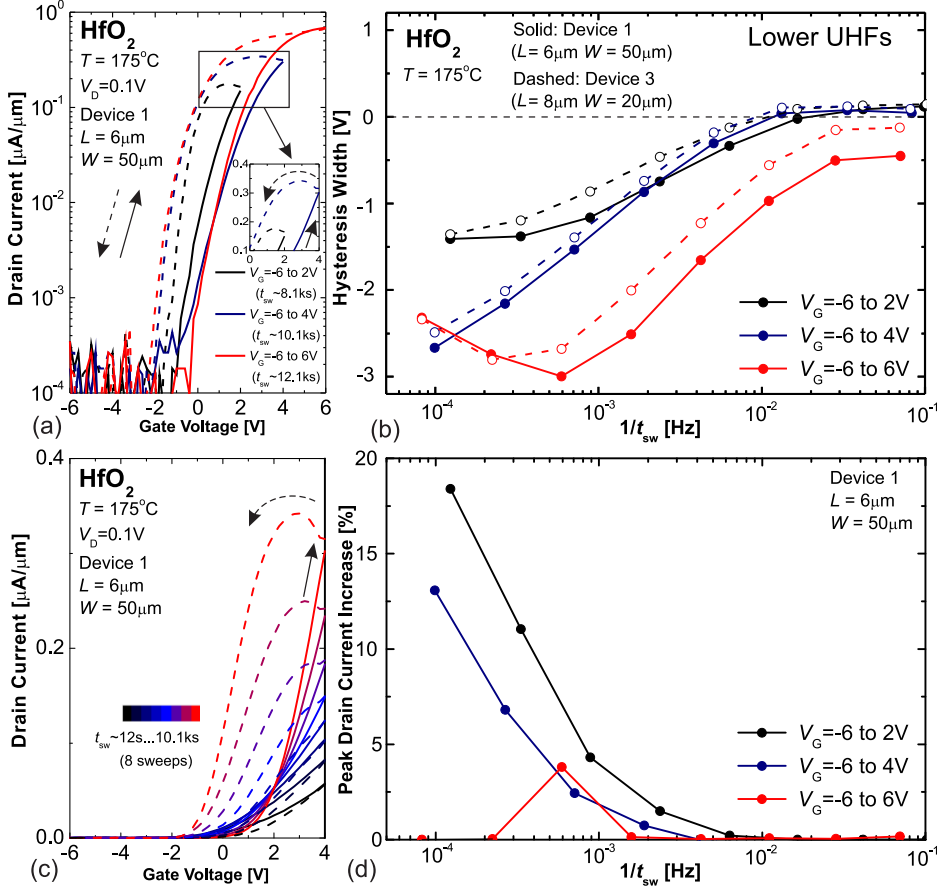


Figure 5: (a) Double sweep I_D - V_G characteristics of the $\text{MoS}_2/\text{HfO}_2$ FET measured using slowest achieved t_{sw} for different V_G sweep ranges and $T = 175^\circ C$. While for -6 to 6 V the CCW hysteresis already starts to localize, for narrower sweep ranges the NDR effect is still present. (b) The lower UHFs obtained for two devices indeed show that for -6 to 6 V the maximum of CCW hysteresis is reached faster which is because with more positive $V_{G\max}$ mobile charges need less time to cross d_{ox} and thus can localize at the channel side of HfO_2 earlier. (c) Full set of double sweep I_D - V_G curves measured using -6 to 4 V sweep range in a linear scale. Sizable and progressive NDR effect towards slower sweeps is visible. (d) The dependence of NDR magnitude vs. sweep frequency for different sweep ranges. Narrower sweep ranges reveal stronger effect that appears at slower sweeps.

frequency dependence of the NDR magnitude quantified as the peak I_D increase relatively to $I_D(V_{G\max})$ of the forward sweep. Indeed, for narrower sweep ranges NDR is stronger and appears in a broader t_{sw} range. This returns us back to the compact model interpretation shown in Fig.4a,b. Namely, when using smaller $V_{G\max}$ we are dealing with the high-mobility NDR effect that is caused by free motion of mobile charges in the bulk of HfO_2 . As in that case the ions mostly do not feel the interface effects, the memory-like performance observed

within a broad range of t_{sw} . Then its magnitude is mostly defined by the proximity of charges to the channel and obviously increases vs. t_{sw} until the states 1' and 2 are reached. However, if V_{Gmax} is more positive, ions pass through the HfO_2 too fast and we likely observe the low-mobility NDR effect related to much slower near-interface motion (state 1'). This type of NDR behavior appears only in a narrow t_{sw} range since at higher V_{Gmax} the state 2 can be reached too fast, thereby making charges immobile. In Fig.S8 in the SI we demonstrate that the key trends related to the impact of V_G sweep range shown in Fig.5 as well as the temperature can be qualitatively captured by our compact model.

We note that classification of the observed NDR mechanisms based on our experimental results and compact model may be useful for future design and precise control of memory dynamics in 2D FETs. For instance, the impact of oxide thickness, interface quality and intentional doping with mobile impurities other than preexisting oxygen vacancies could be discovered.

MoS₂/Al₂O₃ FETs at high temperatures: superior stability

In Fig.6a we show the double sweep I_D-V_G characteristics of our MoS₂/Al₂O₃ FET measured at $T = 175^\circ\text{C}$ using 8 subsequent sweeps with t_{sw} up to 12.1 ks. The corresponding hysteresis mapping results provided in Fig.6b confirm that just like it was at room temperature, purely CW hysteresis is present. However, the results measured for the same device up to $T = 275^\circ\text{C}$ (Fig.6c,d) still allowed us to catch the interplay between the CW and CCW mechanisms (for better understanding, see the full mapping results for all temperatures in Fig.S9 in the SI). Namely, up to $T = 225^\circ\text{C}$ we are dealing with thermally activated charge trapping by oxide traps in Al₂O₃. This results in a well-known decrease of I_D at slow sweeps (Fig.6c and inset) and a classical bell-shape maximum of the CW hysteresis that shifts to faster frequencies vs. temperature.¹⁹ Being rarely observed for amorphous oxides with broad defect bands, here this CW maximum is nicely captured within our t_{sw} range at $T = 225^\circ\text{C}$ (blue curve in Fig.6d). However, at $T = 250^\circ\text{C}$ thermal activation of mobile charges starts that partially

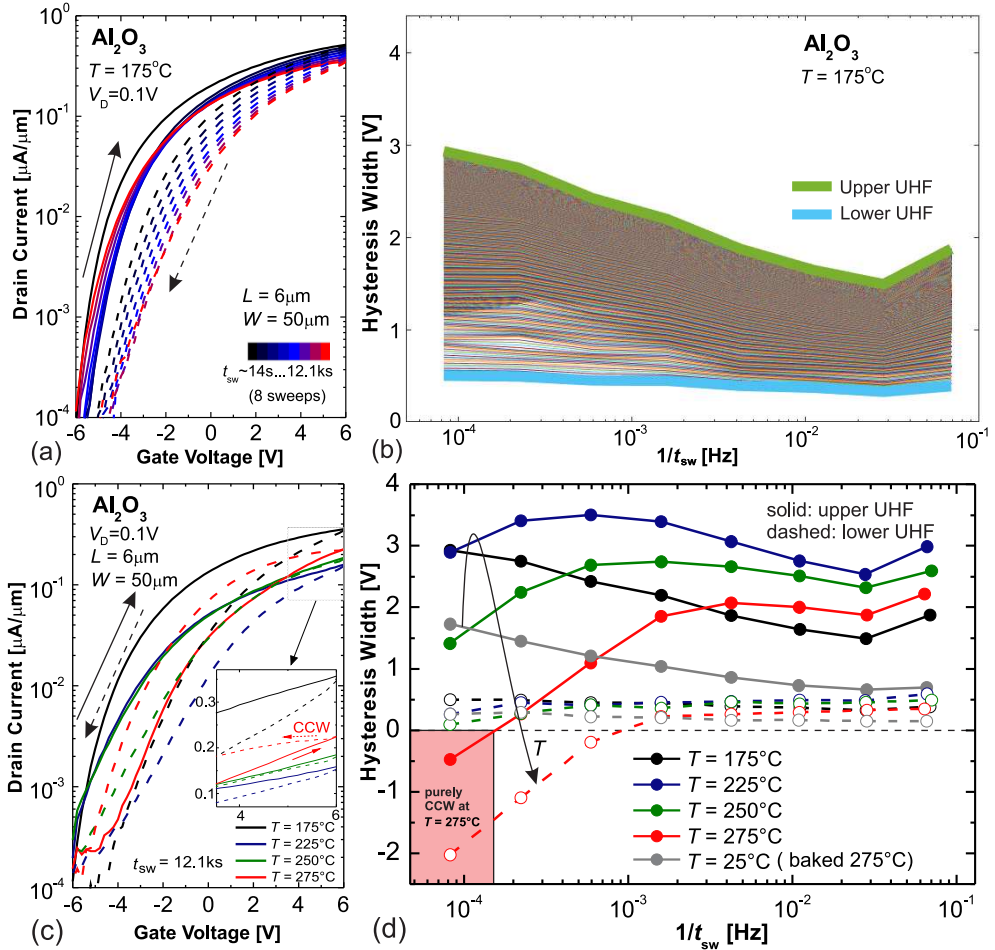


Figure 6: (a) Double sweep I_D - V_G characteristics of our $\text{MoS}_2/\text{Al}_2\text{O}_3$ FET measured at $T = 175^\circ\text{C}$ using 8 subsequent sweeps with t_{sw} up to 12.1 ks. (b) The corresponding mapping results showing that the hysteresis remains purely CW just like it was at room temperature. (c) Double sweep I_D - V_G characteristics measured for the same device up to $T = 225^\circ\text{C}$ using slowest achieved t_{sw} . Transition to the CCW hysteresis at higher temperatures accompanying with slight self-doping is clearly visible. (d) The corresponding upper and lower UHFs showing change from thermal activation of charge trapping up to $T = 225^\circ\text{C}$ to activation of the CCW mechanism related to the drift of oxygen vacancies at higher temperatures. The post-annealing $T = 25^\circ\text{C}$ curves that show smaller and purely CW hysteresis nicely match the trends.

compensates the left part of the CW maximum, and at $T = 275^\circ\text{C}$ we finally see a purely CCW hysteresis at slow sweeps that comes together with the current increase due to self-doping, as was discussed above for the devices with HfO_2 . Remarkably, the $T = 275^\circ\text{C}$ results for this $\text{MoS}_2/\text{Al}_2\text{O}_3$ FET are very similar to those measured for our $\text{MoS}_2/\text{HfO}_2$ device at $T = 125^\circ\text{C}$ (see Fig.S3a,b in the SI). This suggests that the origin of the CCW

hysteresis in both devices is similar, being related to the drift of oxygen vacancies. However, in Al_2O_3 the same CCW effects start to appear for the temperatures that are higher by at least 150°C. Based on our compact model, this suggests that Al_2O_3 should have E_A for migration of oxygen vacancies of about 1.6 eV as compared to 1.15 eV that we assumed for HfO_2 . This may be because ionic Al-O bonds are stronger as compared to Hf-O bonds. Therefore, these results clearly show that Al_2O_3 enables far better stability with respect to the CCW hysteresis caused by drift of oxygen vacancies as compared to HfO_2 , though at the same time being less relevant to achieve NDR memory performance.

Bias stress stability of Al_2O_3 and HfO_2 at high temperatures

To solidify the above findings obtained using hysteresis analysis, we finally examine our $\text{MoS}_2/\text{Al}_2\text{O}_3$ and $\text{MoS}_2/\text{HfO}_2$ FETs under constant bias stress at $T = 175^\circ\text{C}$. These tests focused on tracking the time evolution of I_D up to $t_s = 10\text{ ks}$ at subsequently increased positive stress voltages V_{GS} following 10 ks stabilization at $V_{GR} = 0\text{ V}$, while doing fast control I_D - V_G sweeps before and after each stress. The results for our $\text{MoS}_2/\text{Al}_2\text{O}_3$ devices are shown in Fig.7a,b. Using the fresh reference I_D - V_G curve obtained after initial device stabilization (Fig.7a), we can recalculate the measured $I_D(t)$ traces (Fig.7b, inset) into the $\Delta V_{th}(t)$ dependences (Fig.7b). These results confirm that generally we are dealing with positive ΔV_{th} that originates from charge trapping by oxide traps and cause a decrease of I_D . However, the curves obtained using $V_{GS} = 6\text{ V}$ indicate a clear reversal in the trend with some increase of I_D and thus partial compensation of ΔV_{th} starting at about 1 ks. This suggests activation of slow mobile oxygen vacancies in Al_2O_3 . As was discussed above, they should have larger E_A as compared to the same defects in HfO_2 and thus cannot be captured in hysteresis measurements as the CCW trends would have appeared at inaccessibly slow t_{sw} . Indeed, as illustrated in Fig.6 they introduce the CCW contribution of hysteresis at higher temperatures. We also note that the ΔV_{th} values measured using a constant current mode (Fig.7b) are considerably larger as compared to the ones which we could get

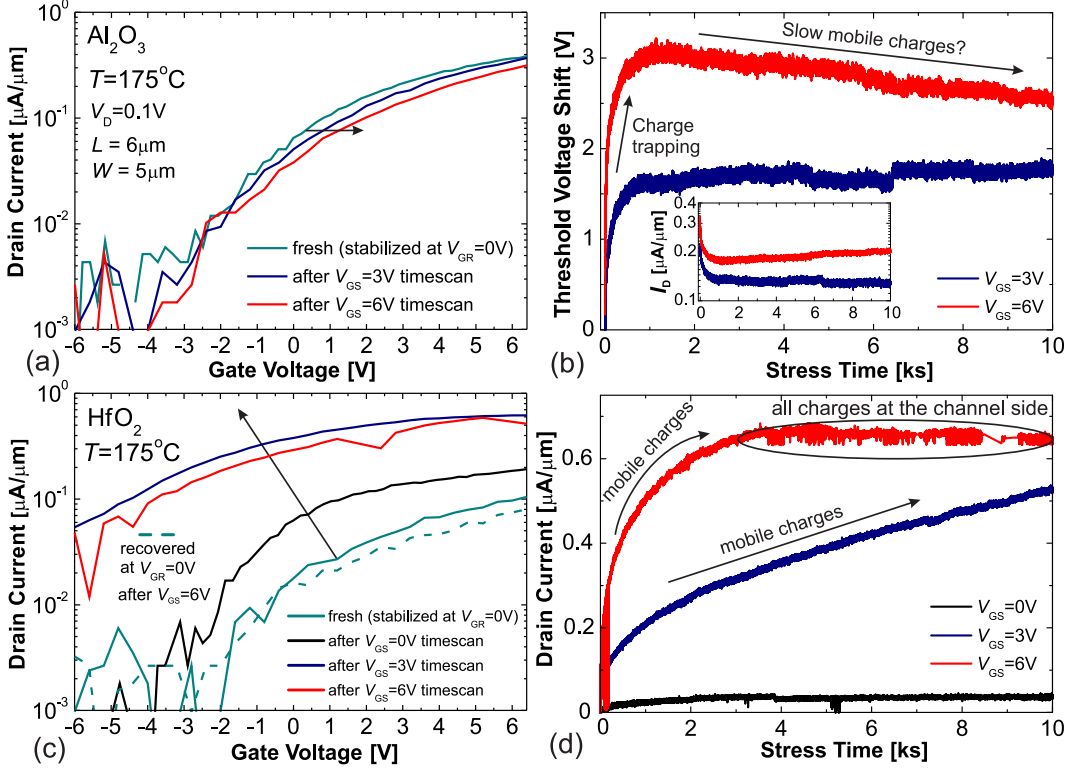


Figure 7: (a) Reference I_D - V_G characteristics of our MoS₂/Al₂O₃ FET measured before and after $t_s = 10\text{ ks}$ gate bias stresses. (b) The ΔV_{th} vs. t_s dependences recalculated from the I_D traces shown in the inset. An increase of positive ΔV_{th} caused by charge trapping is observed, with possible minor signs of reversal for $V_{GS} = 6\text{ V}$ starting from 1 ks that should be due to activation of slow oxygen vacancies in Al₂O₃. (c) Reference I_D - V_G characteristics of the MoS₂/HfO₂ FETs measured before and after $t_s = 10\text{ ks}$ gate bias stresses reveal sizable negative shift of ΔV_{th} that is due to the drift of positive charges to the channel side of HfO₂. (d) The I_D vs. t_s traces clearly show a strong current increase, with possible saturation for $V_{GS} = 6\text{ V}$ when all mobile vacancies reach the channel side of HfO₂. Extraction of ΔV_{th} is barely possible in this case, though its negative sign is obvious.

by comparing the reference curves (Fig.7a). This suggests that the degradation partially recovers already during few seconds of the control I_D - V_G sweeps that is typical for oxide traps at high temperatures.³²

The related results for our MoS₂/HfO₂ FETs provided in Fig.7c,d show a totally different behavior which matches the CCW hysteresis dynamics discussed above. Already from the reference curves (Fig.7c) we see large negative ΔV_{th} after positive bias stresses that comes together with overall increase of I_D . The $I_D(t)$ traces (Fig.7d) also show a strong current

increase that becomes faster and reaches saturation with $V_{GS} = 6$ V. The latter indicates that all charges have reached their equilibrium positions at the channel side of HfO_2 (i.e. state 2 in Fig.4b). However, no recalculation into the $\Delta V_{th}(t)$ dependences is possible since the vertical drifts and transformation of the shapes of I_D - V_G curves make any precise definition of ΔV_{th} impossible. Still in Fig.S10 in the SI we demonstrate that the obtained $I_D(t)$ traces can be qualitatively captured using our compact model for mobile charges with the parameters similar to those used for hysteresis. Furthermore, observations of Fig.7c such as degradation of SS in the post-stress curves and complete recovery after 10 ks at $V_{GR} = 0$ V nicely complement our findings. The former effect can be explained by remote scattering at the positive charges coming closer to the $\text{MoS}_2/\text{HfO}_2$ interface, and the latter one should be due to return of mobile charges back to the gate side of HfO_2 .

Conclusions

In summary, we have performed a detailed comparison of hysteresis dynamics and bias stress stability in $\text{MoS}_2/\text{HfO}_2$ and $\text{MoS}_2/\text{Al}_2\text{O}_3$ FETs fabricated using the same process up to 275°C. Our initial findings indicate that room temperature stability limitations for both device types originate from oxide traps that cause CW hysteresis, with Al_2O_3 showing a slight advantage due to a more favorable fundamental defect band alignment. However, our major results demonstrate that at higher temperatures the devices with HfO_2 exhibit additional severe instabilities which appear as the CCW hysteresis and negative V_{th} drifts under a positive gate bias. This behavior and accompanying I_D increase with possible NDR features can be nicely described by our compact model for mobile charges. The positive oxygen vacancies (V_O^+ or V_O^{2+}) in HfO_2 having migration barriers of about 1 eV are suggested as most likely candidates. Since in Al_2O_3 these vacancies are expected to be slower due stronger ionic bonds, for our $\text{MoS}_2/\text{Al}_2\text{O}_3$ FETs the same effect starts to be pronounced in hysteresis measurements only at 275°C. Our results reveal an essential insulators selec-

tion paradigm for the development and integration of 2D FET technology: while Al_2O_3 is superior to suppress negative V_{th} drifts for high-temperature logic applications, their HfO_2 counterparts can serve as functional active layers that leverage these instabilities to enable intrinsic memory functionality.

Methods

Device fabrication

$\text{MoS}_2/\text{HfO}_2$ and $\text{MoS}_2/\text{Al}_2\text{O}_3$ FETs were fabricated using an identical process employing CVD-grown single-layer MoS_2 films taken from the same batch. Their fabrication process was arranged as follows. First, the Si/SiO_2 substrates were ultrasonically cleaned in acetone and alcohol for 10 minutes each to remove surface contaminants. Local back-gate patterns were then defined via photolithography on the pretreated Si/SiO_2 substrates, followed by deposition of a $\text{Ni}(10\text{ nm})/\text{Au}(30\text{ nm})$ metal stacks as the back-gate electrode using e-beam evaporation. Next, a $\sim 20\text{ nm}$ -thick insulator (HfO_2 or Al_2O_3) was grown via atomic layer deposition (ALD) under optimized process parameters (substrate temperature of 250°C), guaranteeing the homogeneity and interfacial flatness of the insulator. Subsequently, the MoS_2 films were precisely transferred onto the insulator surface via a PMMA-assisted wet transfer method. Residual polymers were removed by acetone and alcohol soaking followed by N_2 blow-drying. The MoS_2 channels were patterned via photolithography and reactive ion etching. Finally, the source/drain contact regions were precisely defined by photolithography. $\text{Ni}(10\text{ nm})/\text{Au}(30\text{ nm})$ was deposited via e-beam evaporation followed by a standard lift-off process, thus completing the back-gate device fabrication.

Electrical characterization

Electrical characterization of $\text{MoS}_2/\text{HfO}_2$ and $\text{MoS}_2/\text{Al}_2\text{O}_3$ FETs was conducted in a vacuum probe station (HCP-O-2, TIANHENG KEYI (SUZHOU) OPTOELEC TECH CO., LTD) with a base pressure of $\sim 5 \times 10^{-6}$ torr. All measurements were performed in complete

darkness over a temperature range from 25°C to 175°C. For electrical measurements we used Keithley 4200A-SCS semiconductor parameter analyzer controlled by a lab-built Python graphical interface to enable uninterrupted long-term testing. Hysteresis dynamics were characterized via double-sweep I_D - V_G measurements with a voltage step of 0.2 V. The sweep time t_{sw} was varied from a few seconds to about 12 ks, and the gate voltage sweep ranges included -6 to 2 V, -6 to 4 V and -6 to 6 V. The hysteresis width was extracted using our universal hysteresis mapping method²⁷ and represented using upper and lower UHFs vs. $1/t_{sw}$. The bias stress analysis was performed by measuring I_D vs. t_s traces up to 10 ks using V_{GS} gradually increased from 0 to 6 V, while applying 10 ks stabilizing rounds with $V_{GR} = 0$ V and doing control I_D - V_G sweeps before each stressing round. Using the initially measured reference I_D - V_G curve, we converted these results into $\Delta V_{th}(t_s)$ dependences for the MoS₂/Al₂O₃ FETs and concluded that it is not possible for the MoS₂/HfO₂ devices due to non-parallel drifts caused by I_D increase.

Compact model

Our compact model describes thermally activated hopping of mobile charges in the oxide with the diffusion coefficient $D = D_0 \exp\left(-\frac{qE_A}{k_B T}\right)$ defined by the activation barrier E_A and constant pre-factor D_0 . Using this diffusion coefficient, we obtain the ion mobility from the Einstein relation and subsequently use it to get their drift velocity under applied gate bias. Next we set the equilibrium positions of positive mobile charges at the gate and channel sides of the oxide for negative and positive V_G , respectively, and apply an iterative scheme to calculate the time-dependent positions of ions $x(t)$ during the sweeps. Finally, knowing $x(t)$ we calculate the resulting ΔV_{th} caused by the drift of mobile charges, and use it for calculation of I_D - V_G curves for different t_{sw} . The model setup is implemented in Matlab. Full description with all equations used can be found in the SI.

Acknowledgement

This work is funded by the National Natural Science Foundation of China (W2432040, 62374155, U25A20496), Guangdong Basic and Applied Basic Research Foundation (2024A1515010179, 2023ZT10X010) and Shenzhen Science and Technology Program (20231115150611001). We also acknowledge the support of the Instruments Center for Physical Science at the USTC and the USTC Center for Micro- and Nanoscale Research and Fabrication.

Author contributions

S.K.Z., H.H.C. and Y.H.W. contributed equally via arranging all measurements and preparing the first draft of the manuscript. Y.F.M. and R.C.Y. fabricated the devices under supervision of Y.Y.S. Y.Z.L. and J.M.H. contributed to hysteresis mapping analysis and data interpretation. Y.Y.I. edited the final manuscript draft, performed compact modeling and supervised the research on electrical characterization.

Competing interests

The authors declare no competing interests.

References

- (1) Uchida, K. and Watanabe, H. and Kinoshita, A. and Koga, J. and Numata, T. and Takagi, S. Experimental Study on Carrier Transport Mechanism in Ultrathin-Body SOI n- and p-MOSFETs with SOI Thickness Less than 5 nm. *IEEE Int. Electron Dev. Meet. (IEDM)*. 2002; pp 47–50.
- (2) Lemme, M.; Akinwande, D.; Huyghebaert, C.; Stampfer, C. 2D Materials for Future Heterogeneous Electronics. *Nat. Commun.* **2022**, *13*, 1392.

(3) Ghosh, S.; Zheng, Y.; Rafiq, M.; Ravichandran, H.; Sun, Y.; Chen, C.; Goswami, M.; Sakib, N. U.; Sadaf, M. U. K.; Pannon, A.; Ray, S.; Redwing, J. M.; Yang, Y.; Sahay, S.; Das, S. A complementary two-dimensional material-based one instruction set computer. *Nature* **2025**, *642*, 327–335.

(4) Schwierz, F.; Pezoldt, J.; Granzner, R. Two-Dimensional Materials and Their Prospects in Transistor Electronics. *Nanoscale* **2015**, *7*, 8261–8283.

(5) Das, S. et al. Transistors Based on Two-Dimensional Materials for Future Integrated Circuits. *Nat. Electron.* **2021**, *4*, 786–799.

(6) Chung, Y.-Y.; Chou, B.-J.; Yun, W.-S.; Hsu, C.-F.; Yu, S.-M.; Chang, Y.-I.; Lee, C.-Y.; Chou, S.-A.; Ho, P.-H.; Wei, A., et al Stacked Channel Transistors with 2D Materials: An Integration Perspective. IEEE Int. Electron Dev. Meet. (IEDM). 2024; pp 1–4.

(7) Mortelmans, W.; Buragohain, P.; Kitamura, A.; Dorow, C.; Rogan, C.; Siddiqui, L.; Ramamurthy, R.; Lux, J.; Zhong, T.; Harlson, S., et al Gate Oxide Module Development for Scaled GAA 2D FETs Enabling $SS < 75\text{mV/d}$ and Record $Id_{max} > 900\mu\text{A}/\mu\text{m}$ at $L_g < 50\text{nm}$. IEEE Int. Electron Dev. Meet. (IEDM). 2024; pp 1–4.

(8) Wachter, S. and Polyushkin, D.K. and Bethge, O. and Mueller, T. A Microprocessor Based on a Two-Dimensional Semiconductor. *Nat. Commun.* **2017**, *8*, 14948.

(9) Huang, J.-K.; Wan, Y.; Shi, J.; Zhang, J.; Wang, Z.; Wang, W.; Yang, N.; Liu, Y.; Lin, C.-H.; Guan, X., et al High- κ Perovskite Membranes as Insulators for Two-Dimensional Transistors. *Nature* **2022**, *605*, 262–267.

(10) Tan, C.; Yu, M.; Tang, J.; Gao, X.; Yin, Y.; Zhang, Y.; Wang, J.; Gao, C., X. Zhang; Zhou, X.; Zheng, L.; Liu, H.; Jiang, K.; Ding, F.; Peng, H. 2D Fin Field-Effect Transistors Integrated with Epitaxial High- κ Gate Oxide. *Nature* **2023**, *616*, 66–72.

(11) Pendurthi, R.; Sakib, N. U.; Sadaf, M. U. K.; Zhang, Z.; Sun, Y.; Chen, C.; Jayachandran, D.; Oberoi, A.; Ghosh, S.; Kumari, S., et al Monolithic Three-dimensional Integration of Complementary Two-Dimensional Field-Effect Transistors. *Nat. Nanotechnol.* **2024**, *19*, 970–977.

(12) Asselberghs, I. et al. Wafer-Scale Integration of Double Gated WS₂ Transistors in 300mm Si CMOS Fab. IEEE Int. Electron Dev. Meet. (IEDM). 2020; pp 40–2.

(13) Dorow, C.; Penumatcha, A.; Kitamura, A.; Rogan, C.; O'Brien, K.; Lee, S.; Ramamurthy, R.; Cheng, C.-Y.; Maxey, K.; Zhong, T.; others Gate Length Scaling beyond Si: Mono-Layer 2D Channel FETs Robust to Short Channel Effects. IEEE Int. Electron Dev. Meet. (IEDM). 2022; pp 7–5.

(14) Jayachandran, D.; Pendurthi, R.; Sadaf, M. U. K.; Sakib, N. U.; Pannone, A.; Chen, C.; Han, Y.; Trainor, N.; Kumari, S.; Mc Knight, T. V., et al Three-dimensional integration of two-dimensional field-effect transistors. *Nature* **2024**, *625*, 276–281.

(15) Fleetwood, D. “Border Traps” in MOS Devices. *IEEE Trans. Nuclear Science* **1992**, *39*, 269–271.

(16) Illarionov, Y.; Knobloch, T.; Jech, M.; Lanza, M.; Akinwande, D.; Vexler, M.; Mueller, T.; Lemme, M.; Fiori, G.; Schwierz, F.; Grasser, T. Insulators for 2D nanoelectronics: the gap to bridge. *Nat. Commun.* **2020**, *11*, 3385.

(17) Knobloch, T.; Waldhoer, D.; Davoudi, M.; Karl, A.; Khakbaz, P.; Matzinger, M.; Zhang, Y.; Smithe, K.; Nazir, A.; Liu, C., et al Modeling the Performance and Reliability of Two-Dimensional Semiconductor Transistors. IEEE Int. Electron Dev. Meet. (IEDM). 2023; pp 1–4.

(18) Provias, A.; Knobloch, T.; Kitamura, A.; O'Brien, K.; Dorow, C.; Waldhoer, D.; Stampfer, B.; Penumatcha, A.; Lee, S.; Ramamurthy, R., et al Reliability Assessment

of Double-Gated Wafer-Scale MoS₂ Field Effect Transistors through Hysteresis and Bias Temperature Instability Analyses. *IEEE Int. Electron Dev. Meet. (IEDM)*. 2023; pp 1–4.

(19) Illarionov, Y.; Rzepa, G.; Waltl, M.; Knobloch, T.; Grill, A.; Furchi, M.; Mueller, T.; Grasser, T. The Role of Charge Trapping in MoS₂/SiO₂ and MoS₂/hBN Field-Effect Transistors. *2D Mater.* **2016**, *3*, 035004.

(20) Karl, A.; Waldhoer, D.; Knobloch, T.; Verdianu, A.; Kurzweil, J.; Bahrami, M.; Davoudi, M. R.; Khakbaz, P.; Stampfer, B.; Sattari-Esfahlan, S. M., et al A standar-dized approach to characterize hysteresis in 2D-materials-based transistors for stability benchmarking and performance projection. *Nat. Commun.* **2025**,

(21) Roh, J.; Lee, J.-H.; Jin, S. H.; Lee, C. Negligible hysteresis of molybdenum disulfide field-effect transistors through thermal annealing. *J. Inf. Disp.* **2016**, *17*, 103–108.

(22) Vu, Q.; Fan, S.; Lee, S.; Joo, M.-K.; Yu, W.; Lee, Y. Near-Zero Hysteresis and Near-Ideal Subthreshold Swing in h-BN Encapsulated Single-Layer MoS₂ Field-Effect Transistors. *2D Mater.* **2018**, *5*, 031001.

(23) Cho, H. W.; Pujar, P.; Choi, M.; Kang, S.; Hong, S.; Park, J.; Baek, S.; Kim, Y.; Lee, J.; Kim, S. Direct growth of orthorhombic Hf_{0.5}Zr_{0.5}O₂ thin films for hysteresis-free MoS₂ negative capacitance field-effect transistors. *npj 2D Mater. Appl.* **2021**, *5*, 46.

(24) Venkatakrishnarao, D.; Mishra, A.; Tarn, Y.; Bosman, M.; Lee, R.; Das, S.; Mukherjee, S.; Talha-Dean, T.; Zhang, Y.; Teo, S. L., et al Liquid Metal Oxide-Assisted Integration of High-k Dielectrics and Metal Contacts for Two-Dimensional Electronics. *ACS Nano* **2024**, *18*, 26911–26919.

(25) Fan, X.; Yi, J.; Deng, B.; Zhou, C.; Zhang, Z.; Yu, J.; Li, W.; Li, C.; Wu, G.; Zhou, X., et al 2D edge-seeded heteroepitaxy of ultrathin high- κ dielectric CaNb₂O₆ for 2D field-effect transistors. *Nat. Commun.* **2025**, *16*, 2585.

(26) Lan, H.-Y.; Yang, S.-H.; Kantre, K.-A.; Cott, D.; Tripathi, R.; Appenzeller, J.; Chen, Z. Reliability of high-performance monolayer MoS₂ transistors on scaled high- κ HfO₂. *npj 2D Mater. Appl.* **2025**, *9*, 5.

(27) Lv, Y.; Cai, H.; Wu, Y.; Illarionov, Y. Y. Mapping diverse hysteresis dynamics in scaled MoS₂ FETs using the universal method derived from TCAD modeling. *arXiv* **2025**, Preprint.

(28) Illarionov, Y.; Knobloch, T.; Waltl, M.; Rzepa, G.; Pospischil, A.; Polyushkin, D.; Furchi, M.; Mueller, T.; Grasser, T. Energetic Mapping of Oxide Traps in MoS₂ Field-Effect Transistors. *2D Mater.* **2017**, *4*, 025108.

(29) Rzepa, G.; Franco, J.; O'Sullivan, B.; Subirats, A.; Simicic, M.; Hellings, G.; Weckx, P.; Jech, M.; Knobloch, T.; Waltl, M.; Roussel, P.; Linten, D.; Kaczer, B.; Grasser, T. Comphy — A Compact-Physics Framework for Unified Modeling of BTI. *Microel. Reliab.* **2018**, *85*, 49–65.

(30) Knobloch, T.; Uzlu, B.; Illarionov, Y.; Wang, Z.; Otto, M.; Filipovic, L.; Waltl, M.; Neumaier, D.; Lemme, M.; Grasser, T. Improving Stability in Two-Dimensional Transistors with Amorphous Gate Oxides by Fermi-Level Tuning. *Nat. Electron.* **2022**, *4*, 98–108.

(31) Bersuker, G.; Gilmer, D.; Veksler, D.; Kirsch, P.; Vandelli, L.; Padovani, A.; Larcher, L.; McKenna, K.; Shluger, A.; Iglesias, V., et al Metal oxide resistive memory switching mechanism based on conductive filament properties. *J. Appl. Phys.* **2011**, *110*.

(32) Illarionov, Y.; Smith, A.; Vaziri, S.; Ostling, M.; Mueller, T.; Lemme, M.; Grasser, T. Bias-Temperature Instability in Single-Layer Graphene Field-Effect Transistors. *Appl. Phys. Lett.* **2014**, *105*, 143507.

Supporting Information

Full mapping results for hysteresis measured at 25°C

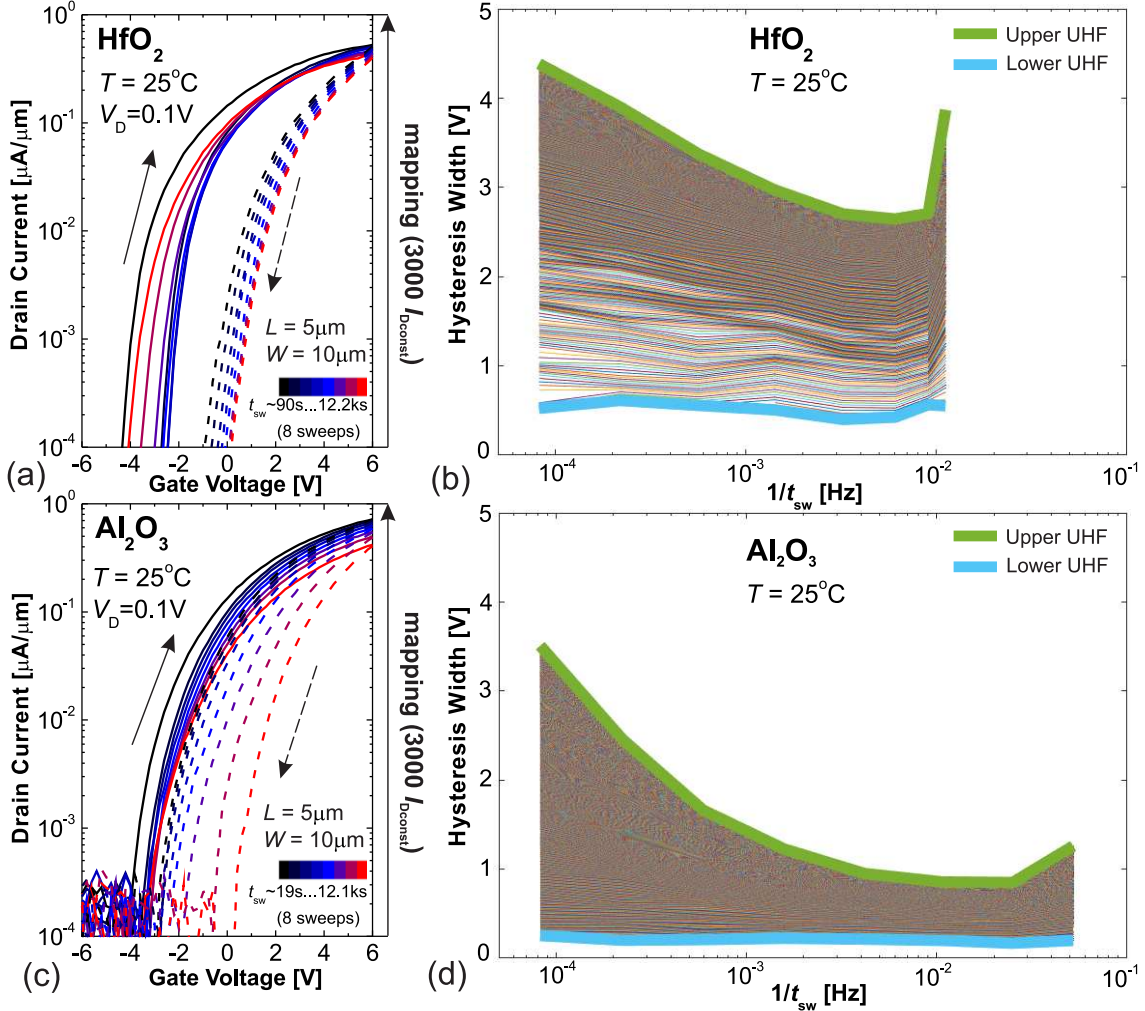


Figure S1: (a) Double sweep I_D - V_G characteristics measured using 8 subsequently increased t_{sw} for our $\text{MoS}_2/\text{HfO}_2$ FET. (b) The corresponding mapping results showing purely CW hysteresis. (c,d) The related results for a representative $\text{MoS}_2/\text{Al}_2\text{O}_3$ FET with the same dimensions. A smaller but still purely CW hysteresis is revealed.

In Fig.S1 we show the full hysteresis mapping results for the representative $\text{MoS}_2/\text{HfO}_2$ and $\text{MoS}_2/\text{Al}_2\text{O}_3$ FETs with the same channel dimensions. By using the measurement datasets consisting of 8 subsequent I_D - V_G sweeps with t_{sw} of up to about 12 ks (Fig.S1a,c), we scan 3000 constant current points and extract series of $\Delta V_H(1/t_{\text{sw}})$ curves. This allows

us to obtain the upper and lower UHFs as shown in Fig.S1b,d. Since in these particular cases the hysteresis is purely CW, only the upper UHFs present practical interest for further analysis. At the same time, consistent representation of the final $\Delta V_H(1/t_{sw})$ dependence as the upper UHF is still of key importance since it is far more accurate as compared to the use of just a single randomly selected $I_{D\text{const}}$ value. As a result, reasonable comparison of hysteresis dynamics measured for different devices becomes possible. For instance, it is obvious that in our case smaller hysteresis in $\text{MoS}_2/\text{Al}_2\text{O}_3$ FETs as compared to their $\text{MoS}_2/\text{HfO}_2$ counterparts is related to the device properties rather than extraction methodology.

Additional results for the temperature dependence of hysteresis in $\text{MoS}_2/\text{HfO}_2$ FETs

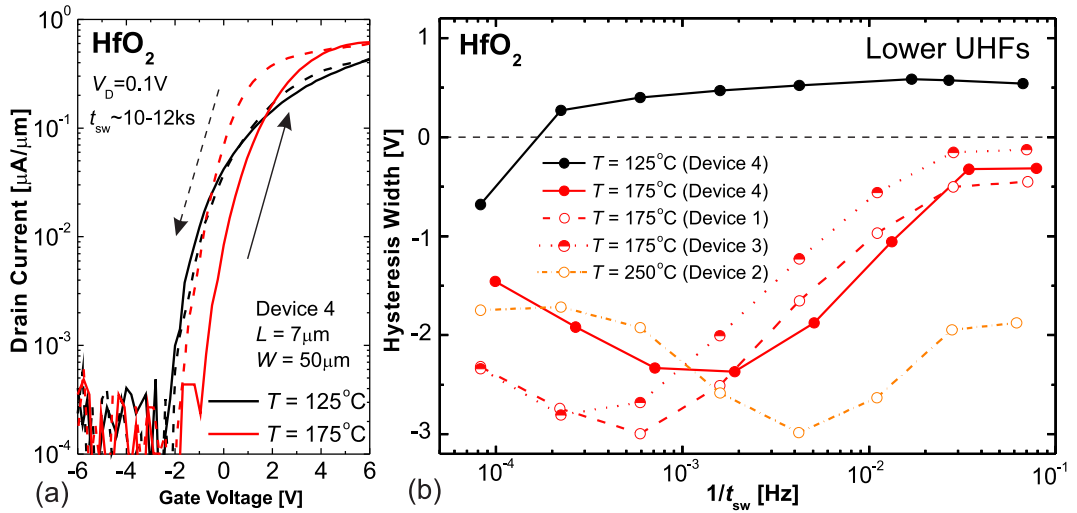


Figure S2: (a) Double sweep I_D - V_G characteristics of the same $\text{MoS}_2/\text{HfO}_2$ FET measured at $T = 125^\circ\text{C}$ and 175°C using slow sweeps. At 125°C only minor signs of the CCW hysteresis appear since mobile charges are too slow. (b) The corresponding lower UHFs (solid lines) confirm strong thermal activation of mobile charges at 175°C and 250°C . This compensates the CW hysteresis coming from charge trapping that is still dominant at 125°C . The 175°C curves for two additional devices (dashed and dotted lines) illustrate that the trends in CCW hysteresis are well reproducible.

In Fig.S2a we show the double sweep I_D - V_G characteristics of the same $\text{MoS}_2/\text{HfO}_2$ FET measured at $T = 125^\circ\text{C}$ and 175°C using slow sweeps. As confirmed by the corresponding lower UHF in Fig.S2b

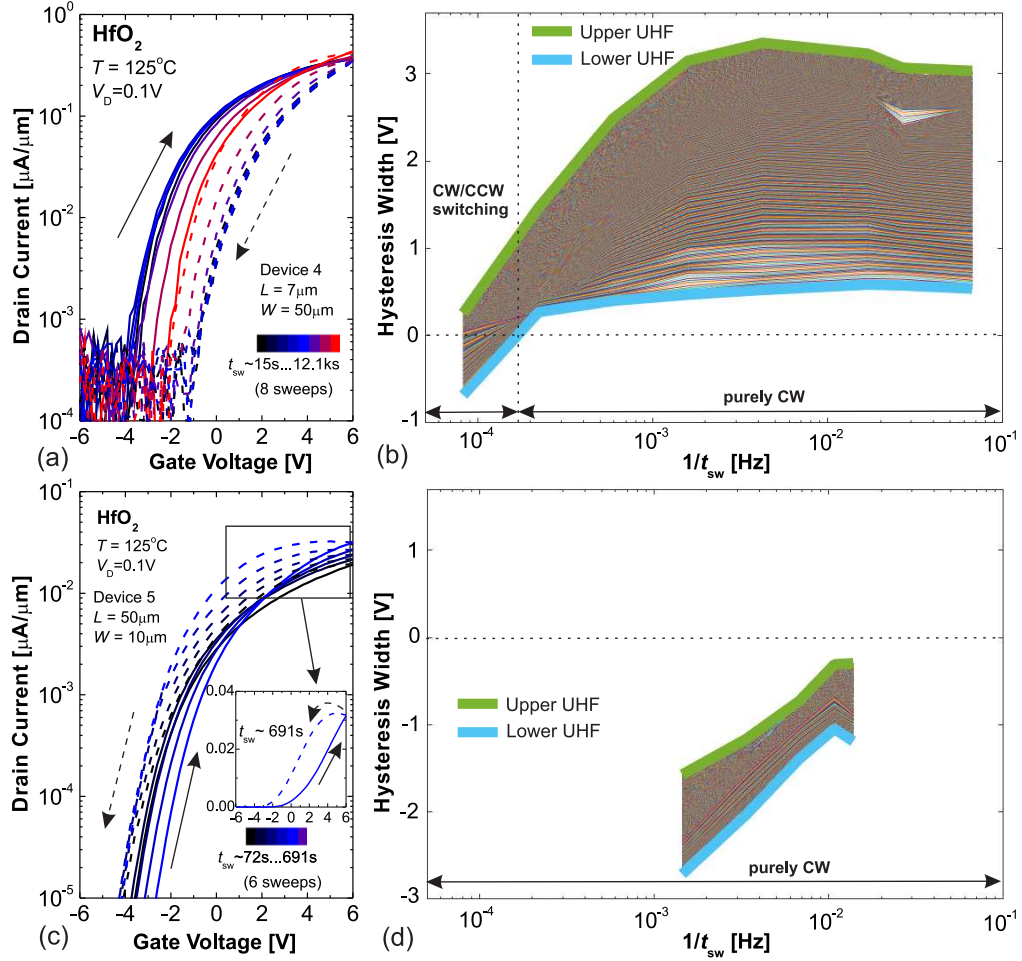


Figure S3: (a) Double sweep $I_{\text{D}}-V_{\text{G}}$ characteristics of our $\text{MoS}_2/\text{HfO}_2$ FET measured at $T = 125^{\circ}\text{C}$ using 8 subsequent sweeps with t_{sw} up to 12.1 ks. (b) Full hysteresis mapping results showing the dominant CW hysteresis with some CW/CCW switching only at slow sweeps. (c,d) More fragmentary results for another device measured at $T = 125^{\circ}\text{C}$ 3 months earlier which show purely CCW hysteresis with NDR at relatively fast sweeps.

the CW hysteresis is still dominant, with only some CW/CCW switching coming into play at about 10 ks sweep time. This indicates that mobile oxygen vacancies are still slow. However, 175°C results for 3 devices showing a distinct maximum of the CCW hysteresis clearly illustrate that this temperature is sufficient to activate mobile charges, and at 250°C the drift of mobile charges is accelerated further.

In Fig.S3a,b we show the full set of $I_{\text{D}}-V_{\text{G}}$ characteristics and the corresponding mapping results measured for the Device 4 from Fig.S2 at $T = 125^{\circ}\text{C}$. As the mobile charges are much slower than at 175°C ,

(Fig.S3c,d) shows purely CCW hysteresis with NDR effects at relatively fast sweeps. According to the modeling results provided in this work, this suggests that the concentration of mobile charges N_{mob} in that device was much higher. However, subsequent storage of the device could result in partial substitution of oxygen vacancies so that in later measurements the same effects with CCW hysteresis become dominant only at higher temperatures. At the same time, some variability in N_{mob} due to different local quality of HfO_2 may be another reason for the observed difference.

Compact model for the CCW hysteresis caused by positive mobile charges

The core physical approach of our compact model is to link the ion mobility in the oxide and the threshold voltage of a MoS_2 FET through a position-dependent electrostatics. This is done by using the following key steps which are implemented into our Matlab script.

Step 1: Incorporate thermally activated hopping of mobile charges

The diffusion coefficient for thermally activated hopping of mobile charges is given as

$$D = D_0 \exp \left(-\frac{qE_A}{k_B T} \right) \quad (4)$$

where D_0 is a pre-factor coefficient and E_A is the energy activation barrier for the migration of ions. Both these parameters play the key role in defining the dynamics of mobile charges in the oxide.

Step 2: Obtain the mobility of ions in the oxide from the Einstein relation

The Einstein relation links the diffusion coefficient and mobility of a charged particle.

Then we can get the following equation for mobility of ions in the oxide

$$\mu = \frac{qD}{k_B T} = \frac{q}{k_B T} \left[D_0 \exp \left(-\frac{qE_A}{k_B T} \right) \right] \quad (5)$$

This makes it possible to convert the random diffusion process into directed drift under

electric field.

Step 3: Obtain drift velocity of mobile charges under gate bias

Knowing the mobility, we can obtain the drift velocity of ions under gate bias which can be represented as

$$v_{\text{drift}} = \mu |E_{\text{ox}}| = \mu \left| \frac{V_{\text{G}}}{d_{\text{ox}}} \right| \quad (6)$$

where the oxide electric field $E_{\text{ox}} = V_{\text{G}}/d_{\text{ox}}$ provides the driving force for ion motion.

Step 4: Determine the time evolution of the position of ions

Ions move to their equilibrium positions (x_{eq}) which is set by the electric field direction in the oxide. Then we consider that under positive V_{G} the equilibrium will be near the channel interface ($x_{\text{eq}} = 0.1 d_{\text{ox}}$), and under negative V_{G} it will be near the gate electrode ($x_{\text{eq}} = 0.9 d_{\text{ox}}$). In that case the actual rate of position change towards equilibrium can be determined as

$$\frac{dx}{dt} = \frac{x_{\text{eq}} - x}{\tau_{\text{drift}}} \quad (7)$$

with the characteristic drift time $\tau_{\text{drift}} = d_{\text{ox}}/v_{\text{drift}}$ representing the time required for ions to cross the oxide. By discretizing the analytical solution of this differential equation, we can obtain the position update of ions at every next time step as

$$dx = (x_{\text{eq}} - x_{\text{current}}) \times \left[1 - \exp \left(-B \frac{dt}{\tau_{\text{drift}}} \right) \right] \quad (8)$$

with the current position x_{current} being considered as the initial position for each step in the loop which states that $x_{\text{new}} = x_{\text{current}} + dx$. Note that considering that the sweeps start at negative V_{G} , for positive charges we use the averaged starting position $0.8d_{\text{ox}}$ at the first step (i.e. close to the gate). The constant parameter B takes into account slowing of ions near the interfaces and their faster motion in the oxide bulk. In our qualitative model setup we use the value of 0.01 if the normalized position of ion $x/d_{\text{ox}} < 0.15$ (i.e. too close

to the channel/oxide interface), 0.03 for $0.15 < x/d_{\text{ox}} < 0.3$, 5 for $0.15 < x/d_{\text{ox}} < 0.85$ and 0.02 for $x/d_{\text{ox}} > 0.85$ (i.e. too close to the gate/oxide interface). The physical meaning of $1/\tau_{\text{drift}}$ is the relaxation rate which thus can be adjusted via multiplying by the position factor B . We note that in principle the diffusion contribution coming from random motion of ions could be added to dx . However, here we assume that the drift caused by applied gate bias has the dominant impact.

Finally, physical constraints $x_{\text{new}} = \max(0.1d_{\text{ox}}, \min(0.9d_{\text{ox}}, x_{\text{new}}))$ are set to prevent non-physical positions that are too close to interfaces which ions cannot occupy due to their finite sizes and interface barriers.

Step 5: Calculation of the threshold voltage shift induced by motion of mobile charges

Knowing the positions of mobile charges at every time step, we next calculate the time-dependent threshold voltage shift which will be induced by their motion in the oxide. It can be written as

$$\Delta V_{\text{th}}(t) = -\frac{Q_{\text{max}}}{C_{\text{ox}}} \left(1 - \frac{x(t)}{d_{\text{ox}}} \right) \quad (9)$$

where $Q_{\text{max}} = qN_{\text{mob}}d_{\text{ox}}$, N_{mob} is the concentration of mobile charges in the oxide and $C_{\text{ox}} = \epsilon_{\text{ox}}\epsilon_0/d_{\text{ox}}$ is the oxide capacitance. The minus sign takes into account that we consider positive charges which should create a negative ΔV_{th} that will have a maximum when all ions accumulate near the channel/oxide interface (i.e. $x = 0$).

Step 6: Calculation of the time-dependent drain current

To calculate the drain current using the obtained ΔV_{th} induced by the ion drift, we first evaluate the interface charge based on the Fermi-Dirac distribution as

$$Q_{\text{it}} = qD_{\text{it}}k_{\text{B}}T \ln \left[1 + \exp \left(\frac{q(V_{\text{G}} - V_{\text{FB}})}{k_{\text{B}}T} \right) \right] \quad (10)$$

where D_{it} is the density of interface states at the channel/oxide interface and the flat band

voltage is determined as

$$V_{FB} = -\phi_b - \frac{E_G}{2} - \frac{qD_{it}E_G}{2C_{ox}} \quad (11)$$

with ϕ_b being the Schottky barrier height at the source/MoS₂ interface and E_G the MoS₂ bandgap.

Then the effective gate voltage which takes into account possible screening by interface charges can be obtained as

$$V_{G,eff} = V_G - \frac{Q_{it}}{C_{ox}} \quad (12)$$

Finally, the ion-induced ΔV_{th} calculated above can be used for piecewise calculation of the drain current as

$$I_D(V_G, t) = \begin{cases} I_{min} \cdot \exp\left(\frac{V_{G,eff} - V_{th} - \Delta V_{th}}{SS}\right) & V_{G,eff} \leq V_{th} + \Delta V_{th} \\ \mu_{eff} \cdot n_{2D} \cdot q \cdot \frac{W}{L} \cdot V_D & V_{G,eff} > V_{th} + \Delta V_{th} \end{cases} \quad (13)$$

where the carrier density is $n_{2D} = C_{eff}(V_{G,eff} - V_{th} - \Delta V_{th})/q$ with effective capacitance $C_{eff} = C_{ox}(C_q + C_{it})/(C_{ox} + C_q + C_{it})$ accounting for the quantum capacitance effects in the MoS₂ channel via $C_q = q^2 m_{eff} / \pi \hbar^2$ and the capacitance of interface states as $C_{it} = qD_{it}$ with m_{eff} being the effective carrier mass in MoS₂ and D_{it} the density of interface states, respectively. The equilibrium threshold voltage V_{th} is set to be 0.5 V above the calculated V_{FB} for simplicity.

Implementation and input parameters of the model

In our Matlab implementation we set the V_G arrays from V_{Gmin} to V_{Gmax} and back and assign the corresponding time point from the time array of 0 to t_{sw} to each V_G point. This obviously makes the results dependent on the input t_{sw} and the V_{Gmin} to V_{Gmax} sweep range so that the hysteresis dynamics observed experimentally could be reproduced qualitatively.

The input material-related parameters of the MoS₂/HfO₂ FETs include the insulator

thickness $d_{\text{ox}} = 20 \text{ nm}$, the permittivity of HfO_2 $\epsilon_{\text{ox}} = 20$, the bandgap of MoS_2 $E_{\text{G}} = 2.53 \text{ eV}$, the Schottky barrier height $\phi_{\text{b}} = 0.2 \text{ eV}$ and the effective electron mass in MoS_2 $m_{\text{eff}} = 0.45 m_0$.

For the simplicity, we also input the minimum current in the OFF state $I_{\text{min}} = 10^{-13} \text{ A}$, effective carrier mobility in MoS_2 $\mu_{\text{eff}} = 10 \text{ cm}^2 \text{V}^{-1} \text{s}^{-1}$ and the subthreshold swing $\text{SS} = 280 \text{ mV/dec}$ to the equation (10). The density of interface states $D_{\text{it}} = -2 \times 10^{12} \text{ cm}^{-2} \text{eV}^{-1}$ is used to consider possible acceptor-type fixed charges at the channel/oxide interface. The drain voltage $V_D = 0.1 \text{ V}$ is set just like in our experiments, as well as the representative channel length $L = 6 \mu\text{m}$ and width $W = 50 \mu\text{m}$.

Finally, the key parameters which determine the dynamics of ion drift in the oxide are the total concentration of mobile charges N_{mob} , the activation energy of their migration E_A and the constant pre-factor D_0 which represents the maximum possible diffusion coefficient if the activation barrier is removed. The best qualitative agreement with our experimentally observed hysteresis dynamics is obtained using $N_{\text{mob}} = 3 \times 10^{19} \text{ cm}^{-3}$, $E_A = 1.15 \text{ eV}$ and $D_0 = 2 \times 10^{-7} \text{ m}^2/\text{s}$. However, for the proof-of-concept demonstrations we also changed these values to illustrate the key trends as specified in the figures.

Impact of N_{mob} and D_0 on the CCW hysteresis dynamics from the compact model

In Fig.S4a we show the double sweep I_D - V_G characteristics of the $\text{MoS}_2/\text{HfO}_2$ FET simulated with our compact model considering a reduced $N_{\text{mob}} = 3 \times 10^{18} \text{ cm}^{-3}$. For this minor concentration of mobile charges in HfO_2 , the CCW hysteresis is small while the self-doping is insufficient to cause any NDR effect or sizable increase of the ON current. However, an obvious kink between the points 1 and 2 is still visible for slow sweeps. This indicates that migration of positive charges to the channel side of HfO_2 still takes place, even though their concentration is small. In contrast, the results simulated with higher $N_{\text{mob}} = 3.6 \times 10^{19} \text{ cm}^{-3}$ (Fig.S4b) reveal a strong NDR effect at moderate sweeps, as well as a more pronounced

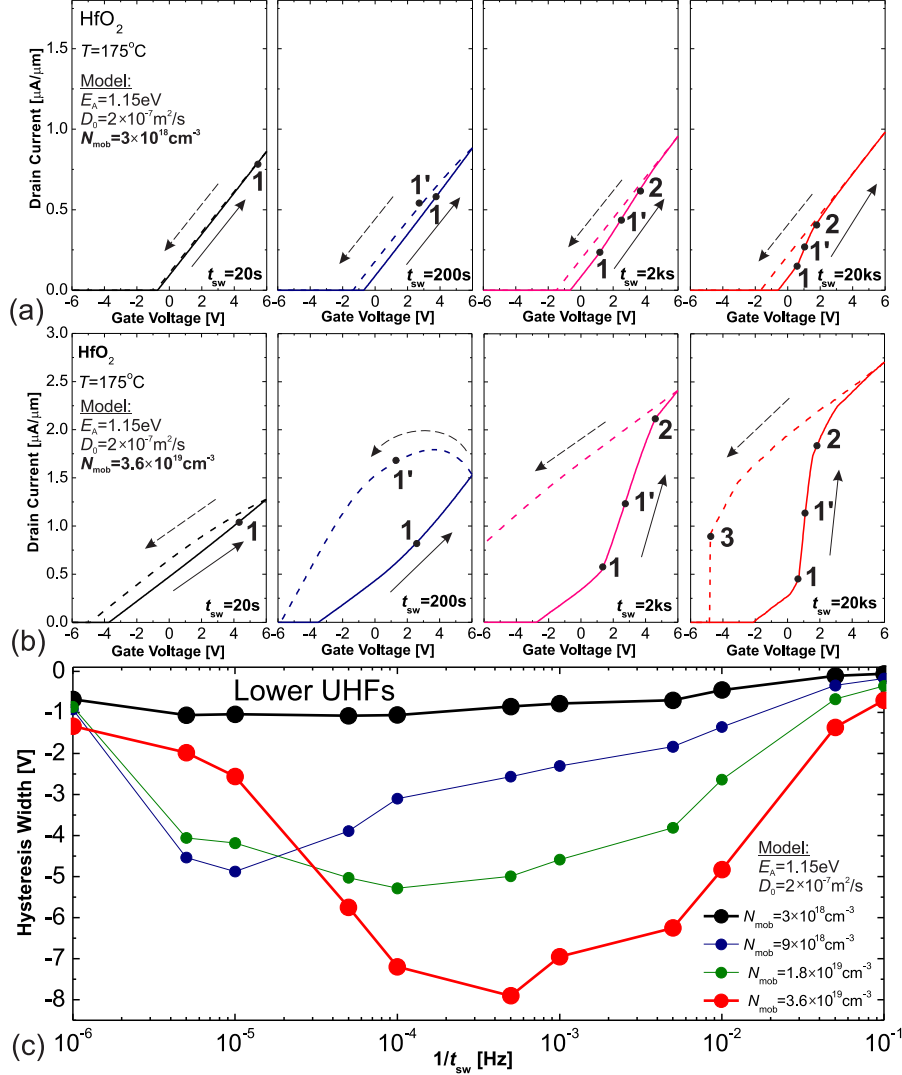


Figure S4: (a) Double sweep I_D - V_G characteristics of the $\text{MoS}_2/\text{HfO}_2$ FET simulated with our compact model considering reduced $N_{\text{mob}} = 3 \times 10^{18} \text{ cm}^{-3}$. No NDR effect is observed while an increase in I_{ON} is minor. (b) The related results obtained using $N_{\text{mob}} = 3.6 \times 10^{19} \text{ cm}^{-3}$. Strong NDR effect is present at moderate t_{sw} . (c) Lower UHFs extracted from the simulation results obtained using different N_{mob} . If there are too many mobile charges in the oxide, the maximum of CCW hysteresis is larger and appears at faster sweeps.

increase of I_{ON} which at slow t_{sw} turns into a large and abrupt kink between the points 1 and 2. In Fig.S4c we show the lower UHFs extracted from the I_D - V_G curves simulated using different N_{mob} . It is obvious that for larger concentrations of ions the CCW hysteresis is larger, while the corresponding maximum is more distinct and appears at faster sweep

frequencies.

In Fig.S5 we show that the pre-factor of the diffusion coefficient D_0 also affects the dynamics of CCW hysteresis considerably. If D_0 is made smaller, the ions obviously become slower and need more time to cross the oxide thickness. This appears in the lower UHFs as a parallel shift of the maximum to slower frequencies. At the same time, D_0 does not affect the shape of the maximum, which is different from the impact of N_{mob} illustrated in Fig.S4c.

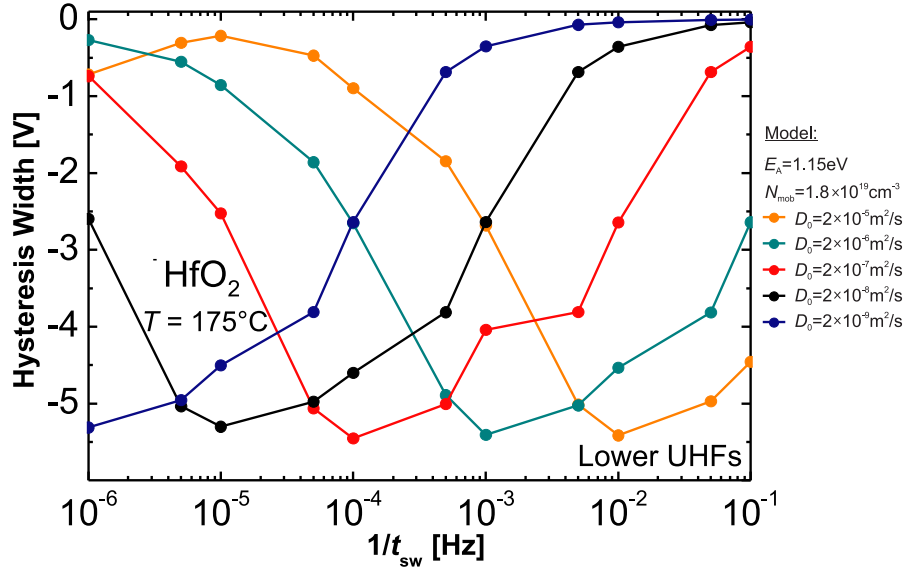


Figure S5: Lower UHFs extracted from the simulation results for the MoS₂/HfO₂ FET obtained using different D_0 . Smaller diffusion pre-factor obviously shifts the maximum of CCW hysteresis to slower sweep frequencies.

Equivalent sets of parameters in the compact model

The dynamics of mobile ions in HfO₂ will be mostly determined by N_{mob} , E_A and D_0 which are not known precisely. While our analysis qualitatively reproduces experimental findings using the Set 1 with $N_{\text{mob}} = 3 \times 10^{19} \text{ cm}^{-3}$, $E_A = 1.15 \text{ eV}$ and $D_0 = 2 \times 10^{-7} \text{ m}^2/\text{s}$, it is obvious that because of several degrees of freedom the compact model can produce identical hysteresis dynamics also using alternative combinations of parameters. Few examples that would be still physically feasible are listed in Fig.S6a and indeed produce the same hysteresis

dynamics as illustrated by the lower UHFs provided in Fig.S6b.

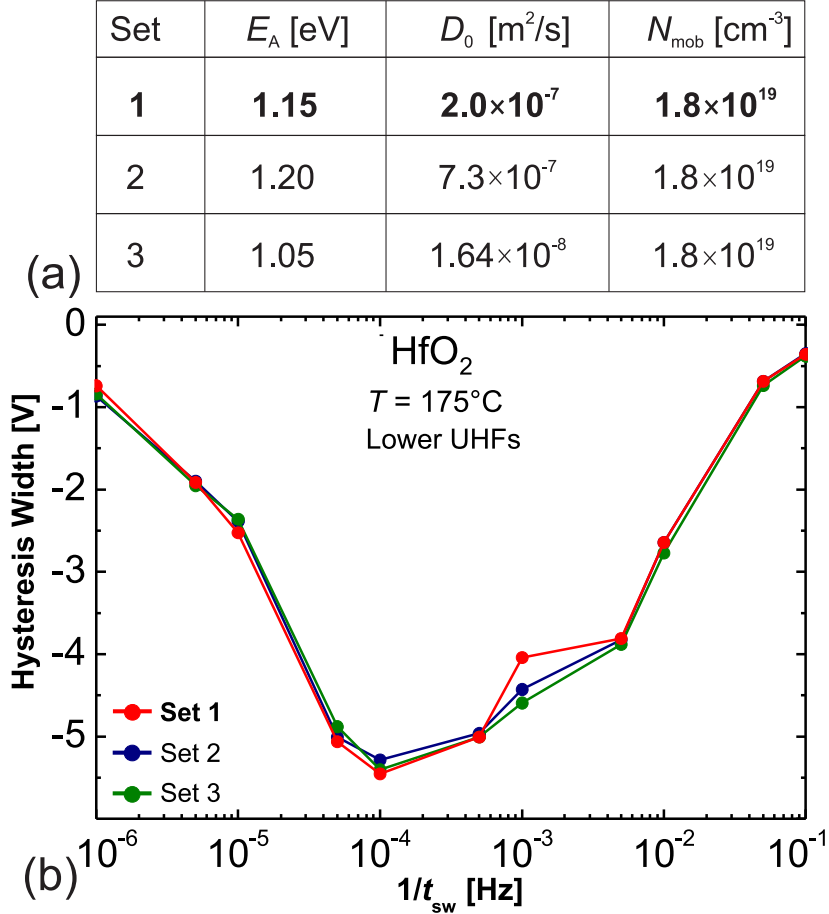


Figure S6: (a) Examples of physically feasible equivalent sets of the key parameters of mobile charges in HfO_2 that would result in identical hysteresis dynamics according to the model. (b) The lower UHFs extracted from the I_D - V_G curves simulated using these 3 parameter sets that indeed look the same.

We see that the model is very sensitive to E_A and even a minor increase of the activation barrier would need a considerably larger D_0 (Set 2). Alternatively, a minor decay in E_A would require a much smaller D_0 to produce the same CCW hysteresis (Set 3). Therefore, we can conclude that considerable deviation of E_A from the range 1.05-1.25 eV that should be typical for oxygen vacancies in HfO_2 would likely result in non-physical values of N_{mob} and D_0 .

Full mapping results for the sweep range dependence of the CCW hysteresis in MoS₂/HfO₂ FETs

In Fig.S7 we provide the full set of I_D - V_G characteristics and the corresponding mapping results measured for our MoS₂/HfO₂ FET at $T = 175^\circ\text{C}$ using different V_G sweep ranges. It is obvious that for narrower sweep ranges NDR effects and CCW hysteresis maximum are observed at considerably slower sweeps. This is because mobile charges in HfO₂ need more time to reach the channel side if $V_{G\text{max}}$ is smaller. As a result, purely CW hysteresis is present for faster sweep frequencies in the case of -6 to 2 V and -6 to 4 V sweep ranges, thereby indicating that mobile charges are still unable to fully compensate charge trapping. Remarkably, with the full mapping results we can clearly identify and separate the frequency ranges with the purely CW hysteresis, CW/CCW hysteresis switching and purely CCW hysteresis.

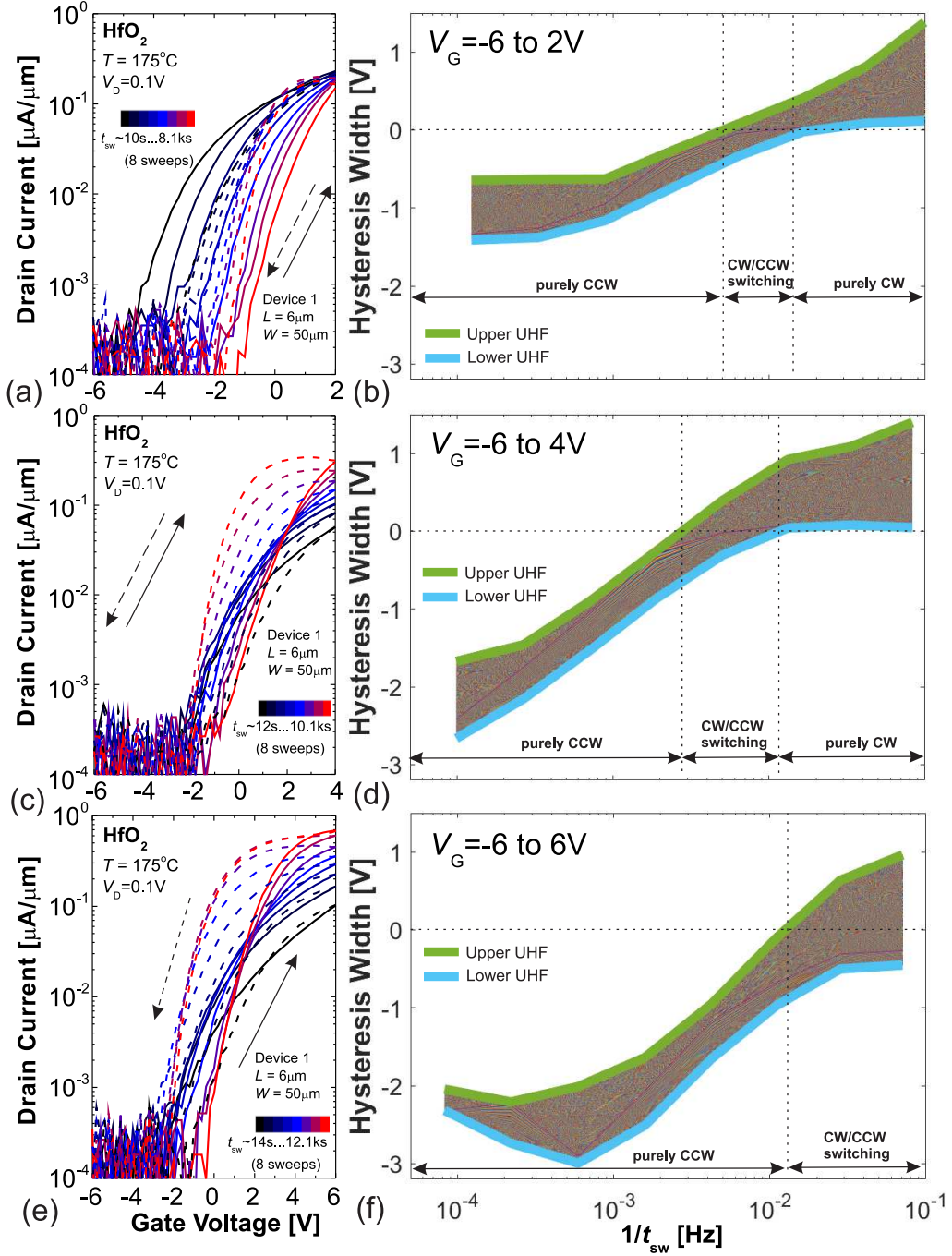


Figure S7: Double sweep I_D - V_G characteristics of our $\text{MoS}_2/\text{HfO}_2$ FET measured at $T = 175^\circ\text{C}$ using 8 subsequent sweeps with t_{sw} up to 8.1, 10.1 or 12.1 ks and full hysteresis mapping results for the sweep ranges of -6 to 2 V (a,b), -6 to 4 V (c,d) and -6 to 6 V (e,f). Frequency ranges with different hysteresis dynamics can be clearly separated based on the signs of the upper and lower UHFs.

Sweep range and temperature dependence of the CCW hysteresis in $\text{MoS}_2/\text{HfO}_2$ FETs: compact model

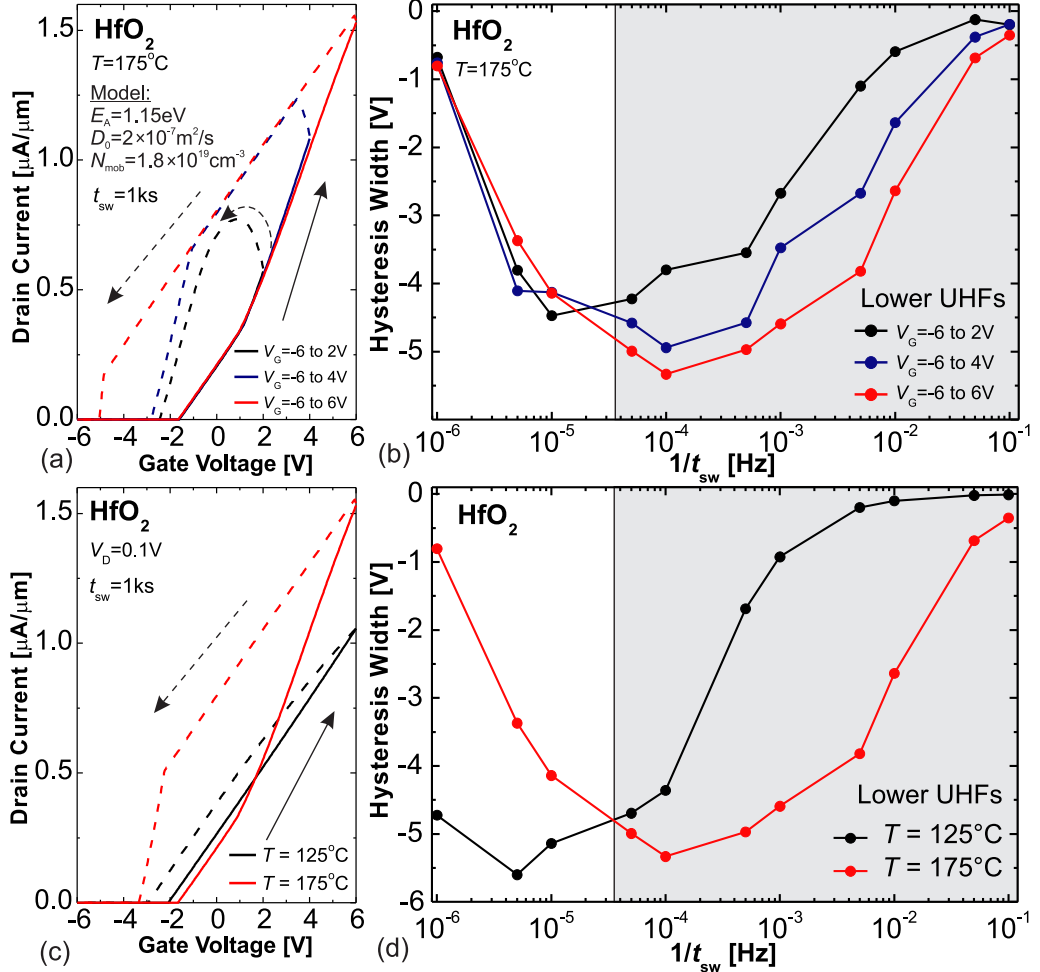


Figure S8: (a) Double sweep I_D - V_G characteristics of the $\text{MoS}_2/\text{HfO}_2$ FET simulated using our compact model while assuming different V_G sweep ranges, $t_{\text{sw}} = 1\text{ ks}$ and $T = 175^\circ\text{C}$. Just like in the experiments, for -6 to 2 V we still observe NDR effect but for -6 to 6 V localization of the CCW starts. (b) The corresponding lower UHF hysteresis also confirm that acceleration of mobile charges with more positive $V_{G\text{max}}$ is well described by the model. (c) Double sweep I_D - V_G characteristics of the $\text{MoS}_2/\text{HfO}_2$ FET simulated with the same model parameters for $T = 125^\circ\text{C}$ and 175°C assuming $t_{\text{sw}} = 1\text{ ks}$. At $T = 175^\circ\text{C}$ the CCW hysteresis is obviously larger. (d) The corresponding lower UHF hysteresis confirm that at higher temperature the CCW hysteresis maximum shifts to faster sweep frequencies.

In Fig.S8a,b we provide the results obtained using our compact model for different V_G sweep ranges. Faster change of the CCW hysteresis from the NDR to localized behavior

for wider sweep ranges observed in the experiments (e.g. Fig.S7) is nicely confirmed by the I_D - V_G characteristics shown in Fig.S8a. The corresponding lower UHFs (Fig.S8b) show that for narrower sweep range the maximum of the CCW hysteresis shifts to slower sweep frequencies, which also goes in line with our experimental findings. Finally, in Fig.S8c,d we show the modeling results for $T = 125^\circ\text{C}$ and 175°C . They nicely confirm that the CCW hysteresis maximum shifts to faster sweep frequencies due to thermal activation of mobile charges which we also observe in our experiments.

Full mapping results for hysteresis in $\text{MoS}_2/\text{Al}_2\text{O}_3$ FETs up to 275°C

In Fig.S9 we provide the full set of I_D - V_G characteristics and the corresponding mapping results measured for our $\text{MoS}_2/\text{Al}_2\text{O}_3$ FET at $T = 175^\circ\text{C}$, $T = 225^\circ\text{C}$, $T = 250^\circ\text{C}$ and $T = 275^\circ\text{C}$. These results show that up to $T = 250^\circ\text{C}$ we are dealing with the purely CW hysteresis which appears as a bell-shape maximum of the upper UHFs that shifts to faster frequencies due to thermal activation. This behavior originates from charge trapping by oxide traps in Al_2O_3 that also causes a typical transformation of the shape of I_D - V_G curves with current decay for slower sweeps. At $T = 250^\circ\text{C}$ a certain compensation of the CW hysteresis at slow sweeps may be present, and finally at $T = 275^\circ\text{C}$ the slow sweep hysteresis is purely CCW. This reveals activation of mobile oxygen vacancies that comes together with the current increase for slow sweeps.

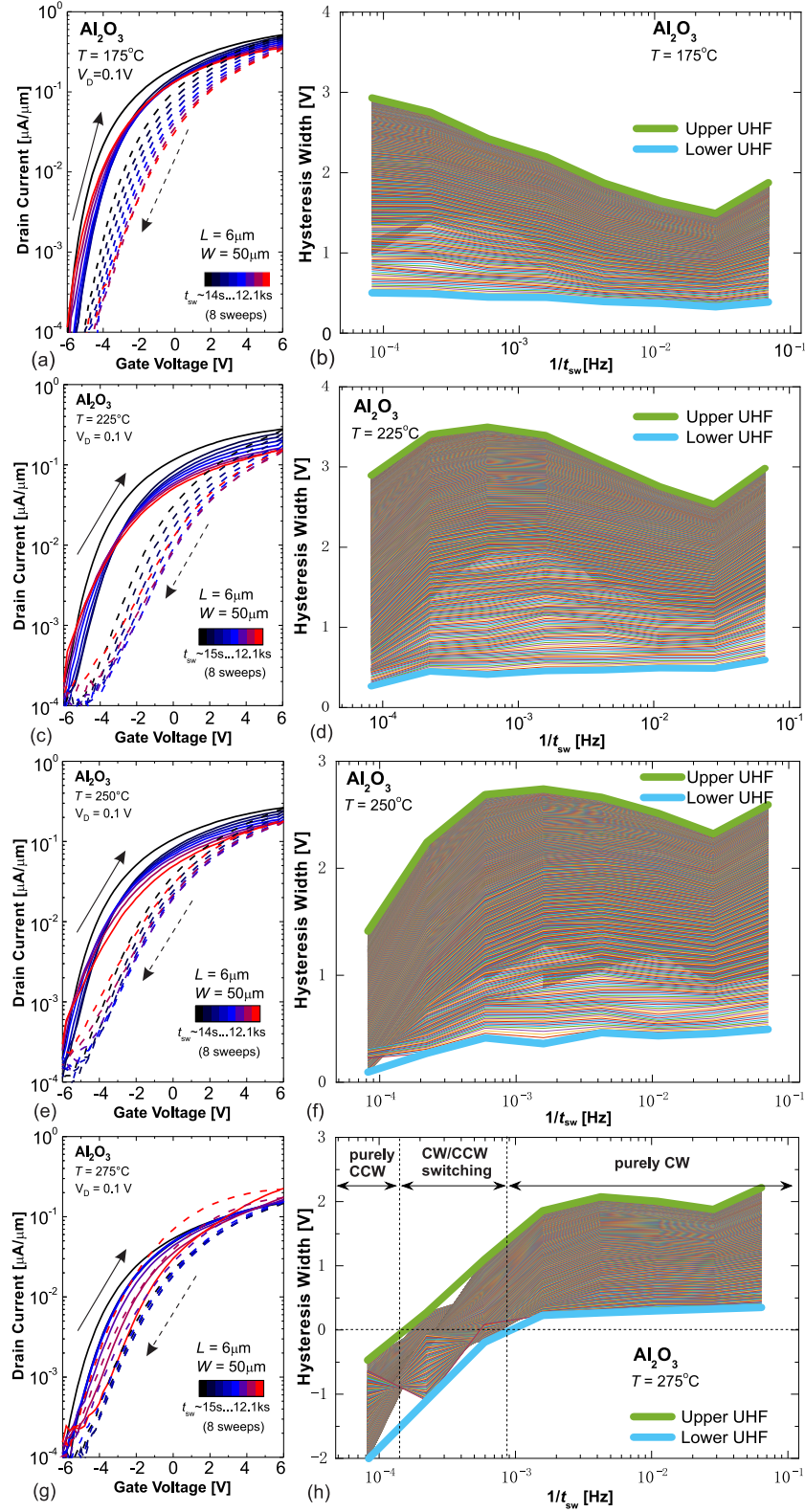


Figure S9: Double sweep I_D - V_G characteristics of our $\text{MoS}_2/\text{Al}_2\text{O}_3$ FET measured using 8 subsequent sweeps with t_{sw} up to 12.1ks and full hysteresis mapping results for $T = 175^\circ\text{C}$ (a, b); $T = 225^\circ\text{C}$ (c, d); $T = 250^\circ\text{C}$ (e, f); $T = 275^\circ\text{C}$ (g, h).

Qualitative modeling of $I_D(t)$ traces for $\text{MoS}_2/\text{HfO}_2$ FETs

In Fig.S10 we show the $I_D(t)$ dependences for a $\text{MoS}_2/\text{HfO}_2$ FET at $T = 175^\circ\text{C}$ obtained using our compact model for mobile charges with the parameters similar to the ones used for hysteresis. The key trends are the same as in our experiments. Namely, the current increases versus time as positive mobile charges come closer to the channel side of HfO_2 . At a certain time saturation of I_D takes place when all of them reach their equilibrium positions. This saturation happens faster if V_{GS} is more positive. However, we note that the initial parts of these traces depend on the starting position of ions input into the simulations, or in fact in their starting distribution in the oxide. Here we consider an averaged value of $0.75d_{\text{ox}}$.

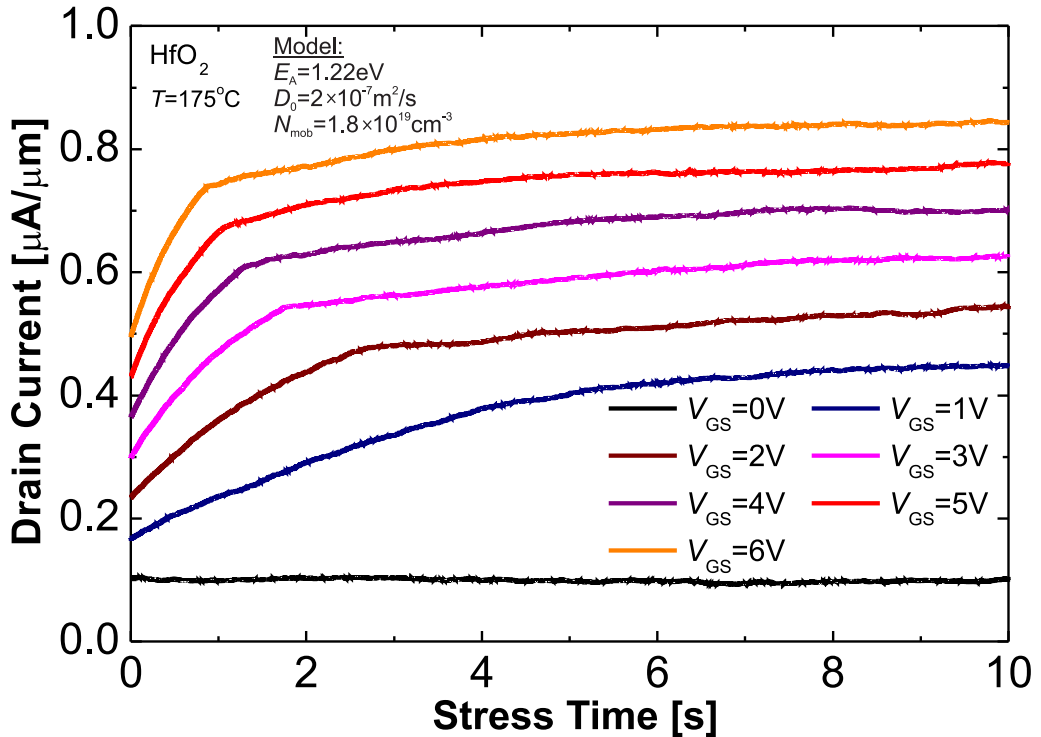


Figure S10: Simulated $I_D(t)$ dependences for a $\text{MoS}_2/\text{HfO}_2$ FET at $T = 175^\circ\text{C}$. Larger V_{GS} makes saturation of I_D faster since mobile charges need less time to cross the oxide.